

A *Swift* X-ray view of the SMS4 sample - II: X-ray properties of 17 bright radio sources.

ALESSANDRO MASELLI ^{1,2} WILLIAM R. FORMAN ³ CHRISTINE JONES ³ RALPH P. KRAFT ³ AND
MATTEO PERRI ^{1,2}

¹*INAF-Osservatorio Astronomico di Roma
via Frascati 33, I-00078, Monte Porzio Catone (Roma), Italy*

²*ASI-Space Science Data Center
via del Politecnico snc, I-00133, Roma, Italy*

³*Harvard-Smithsonian Center for Astrophysics
60 Garden Street, Cambridge, MA-02138, USA*

ABSTRACT

Based on a proposal to observe 18 bright radio sources from the SMS4 catalog with the Neil Gehrels *Swift* Observatory (hereafter *Swift*), we obtained X-ray observations of 17 targets (one target was not observed). Following up our first paper that discussed 31 sources (see Maselli et al. 2022; 20 sources detected as point sources and one very extended source), we present results for this final sample of 17 radio sources, that previously lacked dedicated, pointed narrow FOV X-ray observations. One of these 17 sources, undetected by *Swift* due to a very short exposure, was instead detected by eROSITA, and given in the Data Release 1 (DR1) Catalog. No 1eRASS source was found in the DR1 for the remaining source, unobserved by *Swift*. The new *Swift* observations led to eleven X-ray source detections in the 0.3–10 keV band and six upper limits. We investigated the extent of the X-ray emission, the hardness ratio, and when statistics allowed we carried out a spectral analysis. The X-ray emission of eight sources is consistent with point-like emission, while three sources show clear evidence of extent, each with peculiar properties. We used the X-ray determined positions and uncertainties of the twelve detected sources to establish associations with infrared and optical sources from the AllWISE and the GSC 2.4.2 catalogs. Requiring a detection in both the infrared and the optical bands to establish a candidate counterpart for our X-ray detections, we identify counterparts for all twelve sources. Following this X-ray based approach to derive the position of the active nucleus, we are able to confirm the same IR counterparts previously proposed by White et al. (2020a,b) for eight sources, and provide four new IR candidates. In the optical, we identify counterparts that match the candidates previously given by Burgess & Hunstead (2006a,b) for all sources. We discuss the interesting structure of MRC B0344–345 and PKS B2148–555, two of the six extended X-ray sources that we detected in both our *Swift* campaigns, and suggest they are very promising for further X-ray and radio investigations. For the 38 SMS4 sources that lack pointed, narrow FOV X-ray telescope observations, after our *Swift* campaigns, we list 18 likely counterparts from the eROSITA DR1 catalog.

Keywords: Active galaxies (17) — Extragalactic radio sources (508) — X-ray sources (1810)

1. INTRODUCTION

Bright extragalactic radio sources have been among the most remarkable astronomical targets. For example, Cygnus A, Virgo A, Centaurus A, and Perseus A, have revolutionized our views of how outflows of matter and radiation from supermassive black holes (SMBH) impact the evolution of their host galaxies and their environments, from the first identifications to recent investigations (e.g., Cygnus A - Baade & Minkowski 1954a; Virgo A - Baade & Minkowski 1954b; Churazov et al. 2001; Centaurus A - Schreier et al. 1981; Baade & Minkowski 1954b; Israel 1998;

Perseus A - Lynds 1970; Churazov et al. 2000; Fabian et al. 2000, 2006). As a next step, the first catalogs of radio sources provided an enduring set of targets with key samples for early evolutionary studies (e.g., Lilly & Longair 1984; Laing et al. 1983; Longair & Pooley 1969; Longair & MacDonald 1969) as well as individual objects that have yielded new insights for many decades (e.g., Lilly et al. 1983; Schmidt 1963; Chiaberge et al. 2015; Event Horizon Telescope Collaboration et al. 2019; Hilbert et al. 2016).

As Burgess & Hunstead (2006a) pointed out (see also Dicken et al. 2012 and Massaro et al. 2023a), there is a lack of samples in the southern hemisphere, the site of the newest ground-based telescopes, compared to the flux limited 3C sample (Edge et al. 1959) and its revisions (3CR, Bennett 1962; 3CRR, Laing et al. 1983) of a few hundred objects in the northern hemisphere. To remedy this situation, Burgess & Hunstead (2006a) built the SMS4 sample by extracting sources with flux density S_{408} higher than 4 Jy from the Molonglo Reference Catalogue (MRC; Large et al. 1981). Extrapolating to 178 MHz and matching the 3CRR flux density threshold, they produced a catalog of 137 bright radio sources very similar to 3CRR.

Subsequently, based on observations from the Galactic and Extragalactic All-sky Murchison Widefield Array (MWA; Tingay et al. 2013) survey (GLEAM; Wayth et al. 2015), White et al. (2020a,b) extracted from the GLEAM Extra Galactic Catalogue (EGC; Hurley-Walker et al. 2017) a flux limited sample in the southern hemisphere, the G4Jy, including sources with actual flux density S_{151} higher than 4 Jy. More recently, from the G4Jy catalog, Massaro et al. (2023a) extracted a subset of 264 sources, the G4Jy-3CRE (3CR Equivalent), having a flux limit comparable to that of the 3CR sample.

To characterize bright radio-selected sources from the SMS4 in the X-rays, in 2015 we embarked on an X-ray survey (Maselli et al. 2022) using the Neil Gehrels Swift Observatory (hereafter *Swift*, Gehrels et al. 2004) for all those objects that did not already have good quality X-ray images. Note that our original X-ray program probed the SMS4 radio sample to slightly lower fluxes than the 3C sample.

In Maselli et al. (2022; hereafter Paper I) we reported on *Swift* observations of 31 radio sources selected from the SMS4. In the current paper, we describe an additional sample of 17 targets observed by *Swift* with the X-Ray Telescope (XRT, Burrows et al. 2005). With the XRT, we detect X-ray emission from 11 sources: then, we characterize their extent and the hardness ratio, also carrying out a spectral analysis when statistics allowed. We give upper limits for the remaining six undetected sources, but find for one of these six a 1eRASS source in the DR1 catalog (Merloni et al. 2024) obtained from the first scan of eROSITA data.

As in Paper I, we utilize X-ray observations to provide accurate locations for the central AGN engine of our sources, that were all classified as quasars or radio galaxies in Burgess & Hunstead (2006b). We searched in the AllWISE and GSC 2.4.2 catalogs for sources within the positional uncertainty of the twelve X-ray detected sources, to identify their IR/optical counterparts. We require a detection in both the IR and the optical bands to establish a qualified counterpart, and show their position in $W1$ AllWISE and r DSS2 images. We find an IR/optical counterpart for all the twelve X-ray detected sources, and compare these with candidates previously given in the literature, mainly by White et al. (2020a,b) (hereafter W20) in the infrared and by Burgess & Hunstead (2006a,b) (hereafter BH06) in the optical. With our campaigns, we obtained observations of $\sim 1/3$ SMS4 sources with *Swift*, significantly increasing the *Swift* coverage (see also Massaro et al. 2023b) of powerful radio sources in the southern hemisphere in the last few years.

Throughout this paper we use CGS units, unless otherwise stated. For consistency with Paper I, we also assume a flat cosmology with $H_0 = 72 \text{ km s}^{-1} \text{ Mpc}^{-1}$, $\Omega_M = 0.26$, and $\Omega_\Lambda = 0.74$ (Dunkley et al. 2009).

2. DESCRIPTION OF OUR SAMPLE OF SMS4 SOURCES

Our sample is based on the SMS4 sample, assembled by BH06, and was selected from the 56 SMS4 bright radio sources with no *Chandra*, *Swift*, or *XMM-Newton* observations as of September 2021, that we published in Paper I (see Table 8 therein). For each of the SMS4 sources in that list, a G4Jy source was found, with an unambiguous match. Sorting that list for \bar{S}_{181} , the flux density at 181 MHz derived from W20, we selected and successfully proposed with *Swift* for the 18 brightest radio sources at that frequency, in the range between 12.7 Jy and 34.6 Jy. However, as of May 2024, one source was not yet observed by *Swift* (see Section 3): thus, our sample comprises 17 SMS4 sources.

Using data from the Sydney University Molonglo Sky Survey (SUMSS, Mauch et al. 2003) and the NRAO VLA Sky Survey (NVSS, Condon et al. 1998), at higher frequency than the GLEAM survey, a morphological classification was provided by W20 for all the G4Jy sources, distinguishing single (s), double (d), triple (t), and complex (c) morphology. The main difference between the double and the triple morphology is the capability of detecting what is likely the core

Table 1. Correspondences between the 17 SMS4 sources in our sample and G4Jy sources.

SMS4 Name	S_{178} (Jy)	LAS (arcsec)	z	IAU Name	G4Jy ID	l (deg)	b (deg)	Flux Density (Jy)	Morphology
(1)	(2)	(3)	(4)	(5)	(6)	(7)	(8)	(9)	(10)
B0103–453	19.0	140	(0.71)	J010521–450527	120	295.04	–71.82	17.62±0.02	t
B0202–765	19.0	20	0.38925	J020213–762006	217	297.55	–40.04	14.94±0.01	s
B0242–514	19.0	53	0.791 [†]	J024344–511231	290	269.20	–57.93	13.61±0.02	s
B0344–345	18.0	264	0.0536 [†]	J034631–342238	381	234.94	–51.99	14.61±0.03	t
B0427–366	18.0	14	1.565 [†]	J042940–363050	464	238.77	–43.32	14.73±0.02	s
B1017–426	23.0	10	1.28	J102003–425130	837	275.58	+11.83	21.29±0.02	s
B1526–423	44.0	50	(0.50)	J153014–423146	1262	331.62	+11.32	34.61±0.05	s
B1754–597	20.0	21	(0.8)	J175906–594655	1453	333.77	–17.02	25.16±0.04	s
B1814–519	24.0	10	(0.48)	J181806–515801	1471	342.35	–16.24	23.55±0.03	s
B1817–391	19.0	16	(0.91)	J182035–390925	1474	354.51	–11.26	15.66±0.04	s
B1817–640	28.0	31	0.67	J182216–635915	1477	330.73	–21.12	21.41±0.05	s
B1953–425	33.0	10	(0.12)	J195715–422218	1588	357.49	–29.57	15.90±0.03	s
B2032–350	27.0	26	(0.56)	J203547–345403	1640	7.85	–35.58	23.80±0.04	d
B2041–604	27.0	32	1.464	J204520–601902	1646	336.12	–37.32	20.83±0.03	s
B2140–434	19.0	56	0.648 [†]	J214333–431245	1717	357.25	–49.01	14.70±0.03	d
B2140–817	26.0	44	(0.64)	J214724–813213	1723	310.17	–32.82	12.73±0.04	s
B2331–416	30.0	19	0.907	J233426–412520	1840	345.83	–68.71	23.69±0.03	s
B1827–360*	33.0	10	(0.12)	J183059–360229	1487	358.29	–11.78	30.15±0.04	s

NOTE—The columns show (1) the name in SMS4, according to the MRC designation; (2) the extrapolated flux density S_{178} ; (3) the largest angular size of the radio source at 843 MHz; (4) the redshift values taken from [Burgess & Hunstead \(2006b\)](#) and from [García-Pérez et al. \(2024\)](#), with photometric estimates in parentheses; (5) the International Astronomical Union (IAU) name in G4Jy, according to the GLEAM designation; (6) the G4Jy identifier; Galactic longitude (7) and latitude (8) of the G4Jy source; (9) the actual flux density \bar{S}_{181} for G4Jy; (10) the radio source morphology, following W20 (s=single; d=double; t=triple).

*: this source, included in our original *Swift* proposal, is not part of the sample discussed in this paper since, as of May 2024, it was not observed.

†: this value comes from the spectroscopic campaign described in [García-Pérez et al. \(2024\)](#).

of the radio galaxy, in addition to the lobes; see W20 for further details on their morphology classification criteria. Of the 17 SMS4 sources in our sample, all with a G4Jy counterpart, the radio morphology is triple for 2 sources and is double for 2 sources, with all the remaining sources having a single (compact, substantially symmetric) morphology. These SMS4-G4Jy correspondences are listed in Table 1: quantities in columns 1–4 are taken from BH06, while those in columns 5–10 come from W20.

We used maps from the SUMSS survey, available for all 17 sources, to derive radio flux density contours at 843 MHz. To compare the morphology of the radio source and the underlying X-ray emission, we overlay these contours on the *Swift*-XRT X-ray maps (see Figure 1), generated as described in Section 3. Furthermore, we highlight the distinct SUMSS components encompassed within a circle of radius given by the corresponding Largest Angular Size (LAS) value, reported in Table 1. For each source with multiple components, we assign a letter to each component, sorting them by decreasing flux density (A corresponding to the brighter component). We note that for B0344–345, with a triple morphology (see column 10 in Table 1), we find four SUMSS components within the LAS circle; for B2140–434, with double morphology, three SUMSS components are found; conversely, for B2032–350 just one SUMSS component is found, although the radio source was characterized by a double morphology.

In BH06, for all 17 SMS4 sources making up our sample, an optical counterpart was given using either the plates of the UK Schmidt Southern Sky Survey or R-band CCD images from the Anglo-Australian Telescope (AAT). The spectroscopic redshifts of seven sources, collected from literature, were also reported. For an additional nine sources, photometric redshifts were computed from the magnitudes of the corresponding optical counterparts, using Eq. 2 and Eq. 3 (see their Section 3.8). No redshift measurement was provided for B0427–366.

More recently, [García-Pérez et al. \(2024\)](#) published results from a spectroscopic campaign on G4Jy-3CRE sources, including spectra and redshifts for four of our 17 sources. One of these sources is B0427–366, filling the gap of BH06; the other three sources are B0242–514, B0344–345, and B2140–434. The analysis of [García-Pérez et al. \(2024\)](#) basically confirmed the spectroscopic redshifts already reported by BH06 for B0344–345 ($z = 0.0538$) and B2140–434 ($z = 0.65$), as well as the BH06 photometric estimate for B0242–514 ($z=0.72$). As a result, we have redshifts for all 17 sources in our sample, nine of which are spectroscopic. All these redshift values are reported in Table 1.

3. *Swift*-XRT DATA REDUCTION AND ANALYSIS

The *Swift* campaign described in this paper was organized following a *Swift* proposal (see Paper I) in which we were granted 6 ks exposures, for a total of 108 ks. For each source, the first *Swift* observation started in 2022, between May and December, excluding B1814–519 that was observed in February 2023 for the first time. As of May 2024, the observational campaign was nearly concluded: B1827–360 was the only target still pending any observations, and B1754–597 had a very short exposure. However, all the other sources had a minimum exposure of 2.7 ks, with six sources exceeding the requested exposure time of 6 ks, up to 12 ks for B1817–640.

The X-ray data reduction and procedures adopted in the present analysis are analogous to those already described in Paper I and references therein. Below, we briefly summarize these and include additional details, suited for the present analysis. We give full observational details for detections in Table 2 and upper limits in Table 3 for undetected sources.

X-ray data from the *Swift*-XRT were retrieved from the *Swift* archive and processed with the XRTDAS software package (v.3.7.0), developed at the Space Science Data Center (SSDC) of the Italian Space Agency (ASI) and distributed by the NASA High Energy Astrophysics Archive Research Center (HEASARC) within the HEASoft package (v.6.30.1), including a collection of FTOOLS to manipulate and analyze FITS files. All the XRT observations were carried out in the most sensitive Photon Counting (PC) readout mode. Event files were calibrated and cleaned by applying standard filtering criteria with the XRTPipeline task and using the latest calibration files available in the *Swift* CALDB distributed by HEASARC. In particular, X-ray events are classified according to the charge distribution in a 3x3 matrix of pixels on the detector, following a library of 32 grades: grade 0 is assigned to events with the whole charge concentrated in a single pixel, while increasing grades are due to events with charge progressively spreading to neighbouring pixels, according to a coded scheme¹. Events in the 0.3–10 keV energy range, with grades 0–12, were used in our analysis, and exposure maps were also created with XRTPipeline. For sources with several visits, event files and exposure maps from each observation were accumulated with the XSELECT and XIMAGE tools, respectively, to build a single event file and a single exposure map for each source. Fig. 1 shows the X-ray maps for all 17 SMS4 sources included in our sample, built from the corresponding event files.

One of the observations of B1526–423 (obsID 03111885013) was affected by bright Earth contamination, due to the loading of optical-UV photons, scattered by the Earth’s atmosphere and reflected by the optics of the X-ray telescope onto the XRT detector. Following [Puccetti et al. \(2011\)](#), we checked the background level in this observation and found two peaks in two of its five orbits: thus, we filtered the event file of this sequence removing the bad time intervals during which the background rate over the whole detector was higher than 2 ct s^{-1} , also creating the corresponding exposure map. We checked that no other observation of this source was affected by this issue, before stacking all the observations. No such problem was found for other sources in our sample.

For each source we simultaneously uploaded both the event file and the exposure map within XIMAGE, and used the BACKGROUND command to compute the average background intensity over the whole detector. We checked the background values in the whole 0.3–10 keV band for all sources with sufficient exposure, spanning a range from $4.1 \times 10^{-4} \text{ ct sqarcmin}^{-1} \text{ s}^{-1}$ (B2041–604) to $7.7 \times 10^{-4} \text{ ct sqarcmin}^{-1} \text{ s}^{-1}$ (B1814–519). Excluding sources with $|b| < 20^\circ$, the upper limit of this range decreases to $7.3 \times 10^{-4} \text{ ct sqarcmin}^{-1} \text{ s}^{-1}$ (B2032–350), and yields results consistent with those reported in [Puccetti et al. \(2011\)](#).

We performed a local source detection using the SOSTA command within XIMAGE. This task counts the number of events within a specified box, and corrects these counts for dead time, vignetting, exposure, and Point Spread Function (PSF). As a result, it provides the source intensity and its significance, in terms of the probability P that the signal is a statistical fluctuation of the background. If the probability is higher than $P = 10^{-3}$, a count rate 3σ upper limit is automatically calculated.

¹ For further details, see the *Swift* XRT Data Reduction Guide (https://swift.gsfc.nasa.gov/analysis/xrt_swguide.v1.2.pdf)

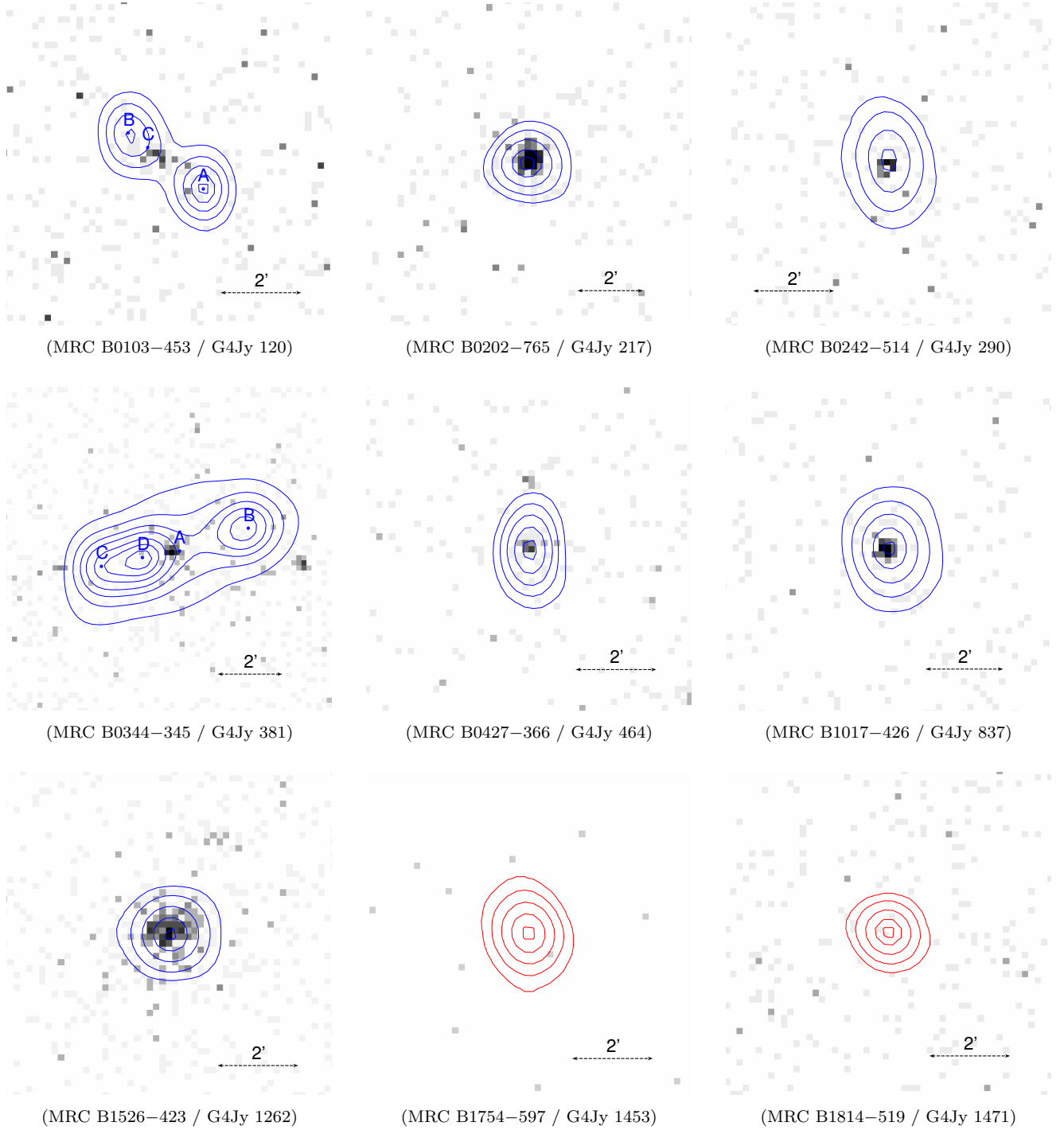


Figure 1. *Swift* X-ray maps (North is up, and East to the left) in the 0.3–10.0 keV band for the 17 sources comprising our sample. All maps, centered at the positions of the SMS4 radio sources, are binned by 4x4 pixels and are 8' x 8' except for B0344–345, shown at 10' x 10'. Radio flux density contours from the SUMSS survey, carried out at 843 MHz, overlay the X-ray maps and have been selected, for each source, to best display the shape of the radio emission. Following Paper I, blue contours distinguish sources detected in the X-rays by *Swift* in our campaign from not detected sources, whose contours are marked in red. B1754–597, not detected in our analysis due to the short exposure, was detected by eROSITA in the 1eRASS scan.

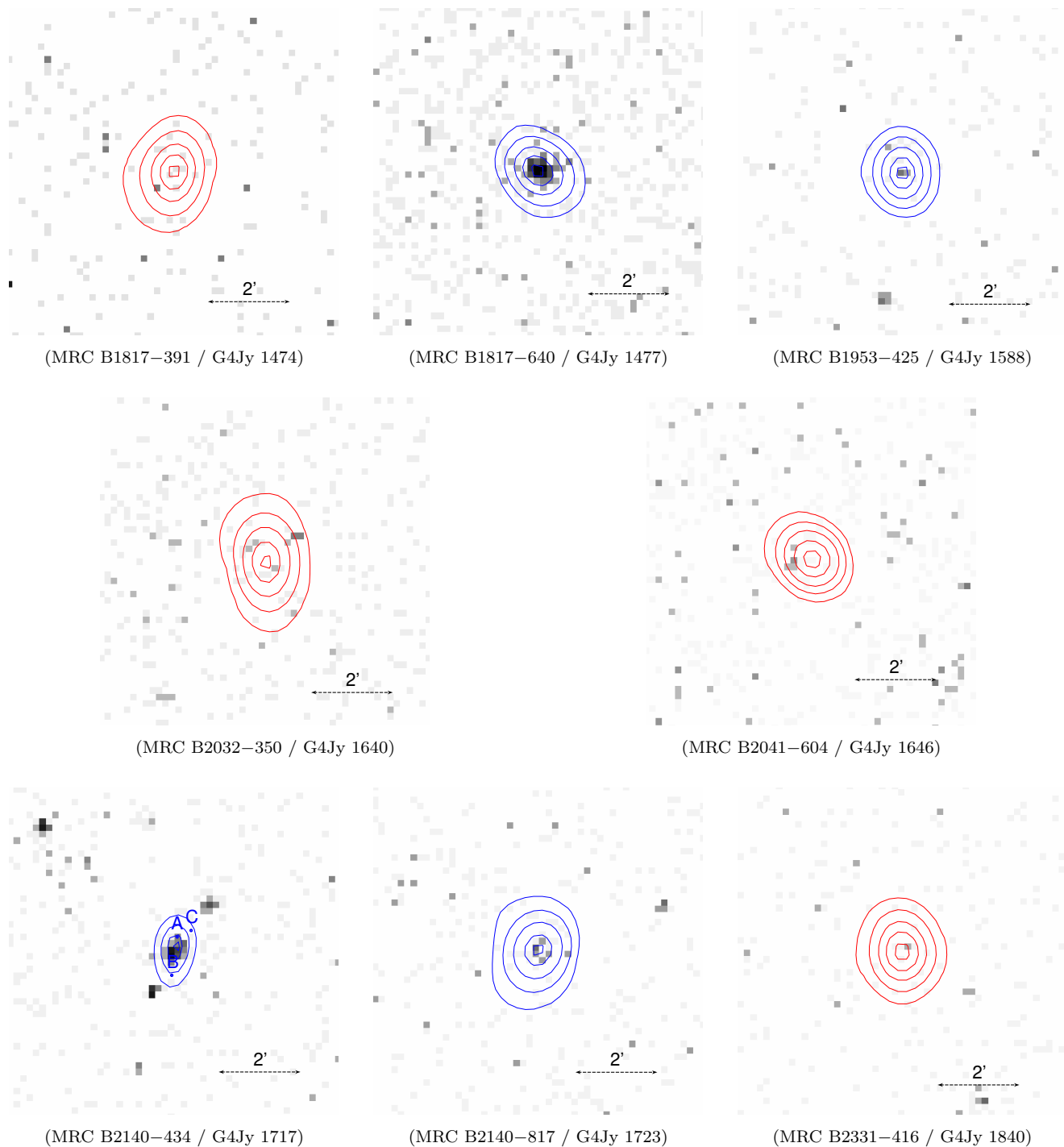


Figure 1. (*continued*)

In our use of SOSTA, the side of the box was fixed to 14 pixels ($\sim 33''$), allowing the core of the PSF to be fully included in the box. Based on our experience in the analysis of XRT images, this choice maximizes the signal-to-noise ratio for faint sources. Furthermore, we used the qualifier `/background_level` to fix the background intensity at the value previously obtained with the BACKGROUND command. Only for B1754-597 was the local background used, since the BACK command in XIMAGE had no effect, presumably due to the extremely short available exposure. For each X-ray image, we used the cursor to precisely center the extraction box on the SMS4 coordinates.

Table 2. Results from *Swift*-XRT observations for the X-ray detected sources of our sample.

R.A. (J2000) (^h ^m ^s)	Decl. (J2000) (^o ['] ^{''})	r_c (arcsec)	Count Rate (10^{-3} ct s ⁻¹)	P (5)	First Obs. (yy-mm-dd)	Latest Obs. (yy-mm-dd)	Obs. (8)	Exposure (s)	SMS4 Name (10)
(1)	(2)	(3)	(4)	(5)	(6)	(7)	(8)	(9)	(10)
01 05 22.3	-45 05 16.9	4.7	2.0 ± 0.7	$6.7 \cdot 10^{-10}$	22-07-26	23-02-19	8	8472	B0103-453
02 02 13.2	-76 20 01.0	3.8	82.8 ± 5.6	$< 10^{-16}$	22-09-01	23-03-19	13	3814	B0202-765 [†]
02 43 44.5	-51 12 39.7	4.8	5.2 ± 1.1	$< 10^{-16}$	22-07-31	24-01-24	6	6952	B0242-514
03 46 30.6	-34 22 47.4	4.0	8.8 ± 1.1	$< 10^{-16}$	22-12-16	23-07-21	10	11019	B0344-345
04 29 40.4	-36 30 52.9	4.8	7.9 ± 1.6	$< 10^{-16}$	22-06-23	23-01-09	4	5009	B0427-366 [†]
10 20 04.2	-42 51 32.5	4.5	15.0 ± 2.1	$< 10^{-16}$	22-12-31	23-06-25	3	4848	B1017-426
15 30 14.3	-42 31 53.7	3.8	23.6 ± 2.6	$< 10^{-16}$	22-05-25	24-01-10	6	5005	B1526-423
18 22 16.1	-63 59 18.6	4.0	11.1 ± 1.2	$< 10^{-16}$	22-08-01	24-02-04	13	12211	B1817-640 [†]
19 57 15.5	-42 22 23.9	5.8	1.7 ± 0.7	$4.0 \cdot 10^{-05}$	23-06-22	23-10-09	7	5390	B1953-425
21 43 33.6	-43 12 50.8	4.3	11.4 ± 1.7	$< 10^{-16}$	22-05-28	22-12-24	18	6288	B2140-434 [†]
21 47 22.7	-81 32 11.3	5.2	4.0 ± 1.1	$8.8 \cdot 10^{-15}$	22-07-23	23-07-18	16	5395	B2140-817
...	22-05-22	24-02-22	2	208	B1754-597*

NOTE—The columns show (1) the Right Ascension and (2) Declination of the X-ray detection; (3) the positional uncertainty r_c , at the 90% confidence level; (4) the 0.3–10 keV count rate, with its uncertainty; (5) the probability P that the signal is a statistical fluctuation of the background; the dates of the first (6) and the latest (7) *Swift* observation; (8) the number of stacked *Swift* observations; (9) the total XRT exposure time at the coordinates of the SMS4 source; (10) the MRC name of the corresponding SMS4 source.

†: The X-ray detection of this source was also reported by [Massaro et al. \(2023b\)](#).

*: This source, not detected in our campaign due to a very short exposure, is reported in the DR1 *Main* catalog ([Merloni et al. 2024](#)) as 1eRASS J175906.4–594643. See also Table 8, where all eROSITA-DE sources matching our detections are listed, with a selection of properties from DR1 catalogs.

Table 3. Results from *Swift*-XRT observations for the X-ray undetected sources of our sample.

SMS4 Name	First Obs. (yy-mm-dd)	Latest Obs. (yy-mm-dd)	Obs. (4)	Exposure (s)	3σ Upper Limit (10^{-3} ct s ⁻¹) (6)
(1)	(2)	(3)	(4)	(5)	(6)
B1814-519	23-02-12	24-05-19	6	3590	4.0
B1817-391	22-07-14	24-02-08	6	2728	6.4
B2032-350	22-09-02	23-04-05	7	5601	2.9
B2041-604	22-08-24	23-10-19	15	7979	2.2
B2331-416	22-08-19	23-04-11	15	5004	4.4
B1754-597*	22-05-22	24-02-22	2	208	45.3

NOTE—The columns show (1) the MRC name of the SMS4 source; the dates of the first (2) and the latest (3) *Swift* observation; (4) the number of *Swift* observations; (5) the total XRT exposure time; (6) the 0.3–10 keV count rate 3σ upper limit at the position of the radio coordinates.

*: This source is also reported in Table 2, since it was detected by eROSITA in the 1eRASS (see Table 8).

Requiring $P < 10^{-4}$, that is an order of magnitude tighter constraint with respect to the default in SOSTA, to establish an X-ray detection, we distinguish detections (Table 2) from non-detections (Table 3). Considering the 17 observed SMS4 sources, our prescriptions led to 11 X-ray detections. To determine the position, and in particular its uncertainty (90% confidence level), for all these detections, we used the XRTCENTROID task.

Table 2 also includes B1754-597, the only source for which we were not able to report a detection due to a very short exposure, and that was instead detected by eROSITA and reported in the *Main* DR1 catalog ([Merloni et al. 2024](#); see Section 3.3 for further details on all the sources in our sample detected by eROSITA).

[Massaro et al. \(2023b\)](#) reported an analysis of *Swift* X-ray observations matching G4Jy-3CRE sources, performed before December 2022 with a minimum exposure of 250 s, yielding a list of 89 G4Jy-3CRE sources observed by *Swift*.

Table 4. X-ray unabsorbed flux and luminosity for the *Swift* detected SMS4 sources of our sample.

MRC Name	D_L (Mpc)	$n_{H, Gal}$ (10^{20} cm^{-2})	XRT Count Rate ($10^{-3} \text{ ct s}^{-1}$)	Power Law Model ($\Gamma = 2$)		APEC Model (0.4 Solar, $kT=3 \text{ keV}$)	
				$S_{0.3-10, unabs}$ ($10^{-12} \text{ erg cm}^{-2} \text{ s}^{-1}$)	L_X (erg s^{-1})	$S_{0.3-10, unabs}$ ($10^{-12} \text{ erg cm}^{-2} \text{ s}^{-1}$)	L_X (erg s^{-1})
(1)	(2)	(3)	(4)	(5)	(6)	(7)	(8)
B0202–765	2068.2	5.5	82.8 ± 5.6	3.35	$1.7 \cdot 10^{45}$	2.77	$1.4 \cdot 10^{45}$
B0242–514	4911.5	2.0	5.2 ± 1.1	0.19	$5.5 \cdot 10^{44}$	0.15	$4.4 \cdot 10^{44}$
B0344–345	233.6	1.1	8.8 ± 1.1	0.31	$2.0 \cdot 10^{42}$	0.28	$1.8 \cdot 10^{42}$
B0427–366	11540.7	1.3	7.9 ± 1.6	0.28	$4.5 \cdot 10^{45}$	0.21	$3.4 \cdot 10^{45}$
B1017–426	8972.6	7.8	15.0 ± 2.1	0.64	$6.2 \cdot 10^{45}$	0.50	$4.8 \cdot 10^{45}$
B1817–640	3997.3	6.8	11.1 ± 1.2	0.46	$8.8 \cdot 10^{44}$	0.37	$7.0 \cdot 10^{44}$
B2140–434	3850.5	1.5	11.4 ± 1.7	0.41	$7.3 \cdot 10^{44}$	0.33	$5.9 \cdot 10^{44}$
B0103–453	4294.7	1.6	2.0 ± 0.7	0.07	$1.6 \cdot 10^{44}$	0.06	$1.3 \cdot 10^{44}$
B1526–423	2793.4	8.7	23.6 ± 2.6	1.03	$9.6 \cdot 10^{44}$	0.83	$7.7 \cdot 10^{44}$
B1953–425	546.1	5.2	1.7 ± 0.7	0.07	$2.4 \cdot 10^{42}$	0.06	$2.1 \cdot 10^{42}$
B2140–817	3777.6	8.3	4.0 ± 1.1	0.17	$3.0 \cdot 10^{44}$	0.14	$2.4 \cdot 10^{44}$

NOTE—The columns show (1) the name of the SMS4 source; (2) the luminosity distance D_L , computed using the redshift values given by BH06 and [García-Pérez et al. \(2024\)](#); (3) the Galactic hydrogen column density in the direction of the X-ray source; (4) the count rate detected by the XRT, as reported in Table 2; (5) the unabsorbed flux in the 0.3–10 keV band derived by WebPIMMS, assuming a power-law model with photon index $\Gamma = 2$, with (6) the corresponding luminosity in the 0.3–10 keV band; (7) the same as column (5), but assuming an APEC model with a metal abundance corresponding to 0.4 Solar and a plasma temperature $kT = 3 \text{ keV}$, with (8) the corresponding luminosity in the 0.3–10 keV band. Sources are distinguished according to spectroscopic (top) and photometric (bottom) redshift measurements.

Due to their selection criteria, [Massaro et al. \(2023b\)](#) include only eight of the 17 sources in our sample, and detect only four of the sources given in Table 2.

We used the count rate values reported in Table 2 to compute the X-ray flux and luminosity in the 0.3–10 keV band of the 11 XRT detected sources. This was allowed after confirming all the optical counterparts quoted by BH06 and [García-Pérez et al. \(2024\)](#) (see Section 4), and using the redshift values reported in their study. As shown in Table 1, there are seven sources with spectroscopic redshifts, and photometric redshifts for the remaining four. For each source, we computed the luminosity distance and used WebPIMMS to convert the XRT count rate into unabsorbed flux in the 0.3–10 keV band. We used two different spectral models, both absorbed by the Galactic hydrogen column density, to take into account two different emission mechanisms: a power law with photon index $\Gamma = 2$ for AGN point-like sources and an APEC model (0.4 Solar abundance, $kT=3 \text{ keV}$) for thermal emission from a diffuse source. The results of our analysis are reported in Table 4.

3.1. Extent and Shape of the X-ray Emission

After detecting an X-ray source, the extent and surface brightness distribution can provide key details. For each X-ray detected source, we compared the radial distribution of the detected events with that expected from a point-like source. We based such a comparison on the analytic PSF model for the *Swift*-XRT telescope, as derived by the XRT Calibration Team (https://heasarc.gsfc.nasa.gov/docs/heasarc/caldb/swift/docs/xrt/SWIFT-XRT-CALDB-10_v01.pdf), given by the sum of a Gaussian and a King law. Since most of the events are found at $\sim 1.5 \text{ keV}$, where the XRT effective area peaks, we adopted the parameters corresponding to the on-axis PSF at this energy value. We also note that the dependence of the PSF profile on energy is mild ([Moretti et al. 2005](#); https://heasarc.gsfc.nasa.gov/docs/heasarc/caldb/swift/docs/xrt/SWIFT-XRT-CALDB-10_v01.pdf).

Our analysis of source extent was carried out in two steps. First, a ratio test, described in Section 3.1.1, is given by the comparison of the number of events in a circle C and a surrounding annulus A centered on the X-ray centroid; these regions are shown for example in Figure 2. Next, for those sources showing clear evidence of extent from the ratio test, we computed their radial profile, as described in Section 3.1.2, and compared it with the analytic *Swift* PSF model.

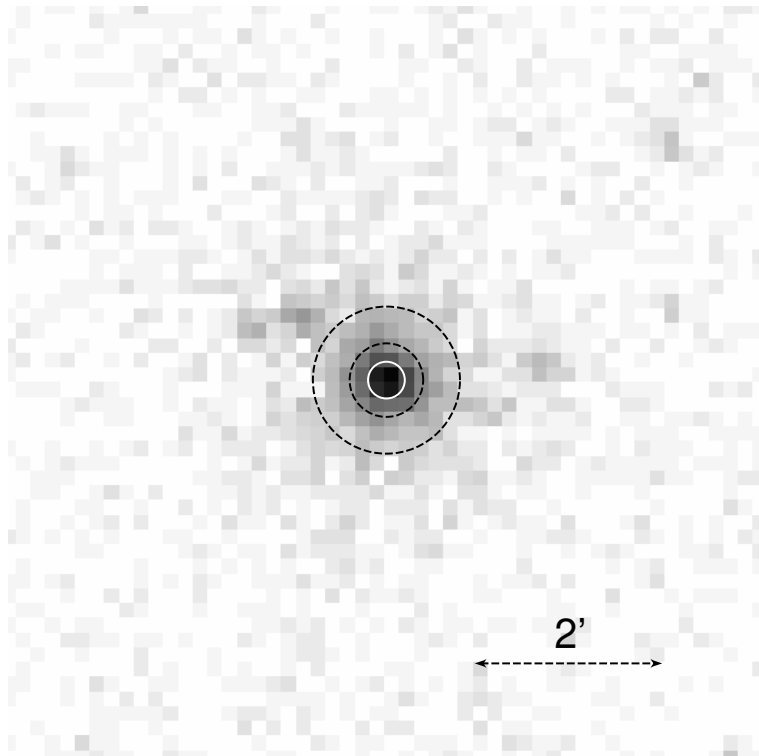


Figure 2. *Swift* X-ray map (N is up, and E to the left) in the 0.3–10.0 keV band of MRK 876, a calibration point source with an exposure of 48795 s. The radius of the white circle C is 5 pixels (1 pixel = $\sim 2''.36$), while the inner and the outer radii of the black dashed annulus A are 10 and 20 pixels, respectively. The map is binned by 4x4 pixels.

To verify our procedure we used MRK 876, a Seyfert 1 galaxy, that was used by the *Swift* team as a point-like source for its first in-flight calibration of the PSF (Moretti et al. 2005)² and that has been repeatedly observed by XRT since its launch, achieving a remarkably deep exposure. We note that Chandra observations, from 2016–2017, of MRK 876 are fully consistent with it being an unresolved source. First, MRK 876 shows strong variability (40%) on time scales of months (see Fig. 8 of Bottacini 2022). Second, we have merged the 12 Chandra observations and find no structure beyond one single source (14949 counts with 10 background in the energy band 0.6–3.0 keV). We find an encircled energy of 95% (within $2''$, in the energy band 0.6–3.0 keV), which agrees with that of the Chandra PSF calibration (Chandra POG³, see Sections 4.2.3 and 6.6).

3.1.1. Ratio Test for Source Extent

Following Paper I, we used as extraction regions for our analysis (see Figure 2) a circle C with a radius of 5 pixels ($\sim 12''$) for the source and an annulus A with inner and outer radii of 10 and 20 pixels, respectively, for the background. Both regions are centered at the coordinates of each X-ray centroid, given in Table 2. We verified that the annulus did not include any spurious X-ray sources. Unlike Paper I, which used only the broad band (0.3–10.0 keV), we also carried out our analysis in the 0.5–4 keV band to focus more on thermal emission, appropriate to groups and clusters. After extracting the counts from the circles C and the annuli A , we corrected them for the background contribution, computed as reported in Section 4.

The fraction $ER = C/A$ expected from a point-like source, computed from the analytic PSF model, is equal to 5.73. Thus, a deviation from this value reveals that the distribution of events differs from that expected from a point-like source, making ER a marker of extended X-ray emission. The ER values of the X-ray detected sources, for both the 0.5–4 keV and the 0.3–10 keV bands, are reported in Table 5.

According to the results in Table 5, B0103–453 and B1526–423 show clear evidence of extended emission, with ER values lower than 5.73 at very high statistical significance; for B1526–423, $ER < 5.73$ by more than 40σ in both

² The document can be also retrieved at <https://heasarc.gsfc.nasa.gov/docs/heasarc/caldb/swift/docs/xrt/index.html>

³ <https://cxc.cfa.harvard.edu/proposer/POG/>

Table 5. Extent of the X-ray emission.

Source Name	0.5–4 keV Band				0.3–10 keV Band			
	Background (10^{-2} ct/px)	C (ct)	A (ct)	ER	Background (10^{-2} ct/px)	C (ct)	A (ct)	ER
(1)	(2)	(3)	(4)	(5)	(6)	(7)	(8)	(9)
B0103–453	0.28	2	15	0.13 ± 0.13	0.62	9	15	0.60 ± 0.35
B0202–765	0.17	142	25	5.68 ± 1.61	0.34	174	27	6.44 ± 1.73
B0242–514	0.26	13	4	3.25 ± 2.53	0.58	17	7	2.43 ± 1.51
B0344–345	0.44	51	19	2.68 ± 0.99	0.82	59	25	2.36 ± 0.78
B0427–366	0.22	22	8	2.75 ± 1.56	0.38	25	8	3.13 ± 1.73
B1017–426	0.21	34	4	8.50 ± 5.71	0.36	42	8	5.25 ± 2.67
B1526–423	0.41	35	82	0.43 ± 0.12	0.63	38	95	0.40 ± 0.11
B1817–640	0.67	48	14	3.43 ± 1.41	1.22	66	27	2.44 ± 0.77
B1953–425	0.26	4	4	1.00 ± 1.00	0.45	4	3	1.33 ± 1.44
B2140–434	0.27	26	7	3.71 ± 2.13	0.52	36	10	3.60 ± 1.74
B2140–817	0.24	8	3	2.67 ± 2.48	0.49	9	6	1.50 ± 1.11
Point-like Source Test								
MRK 876 (90 s)	0.04	11	3	3.67 ± 3.22	0.05	14	4	3.50 ± 2.69
MRK 876 (276 s)	0.02	31	6	5.17 ± 3.04	0.02	34	8	4.25 ± 2.23
MRK 876 (1000 s)	0.03	130	26	5.00 ± 1.42	0.07	178	36	4.94 ± 1.19
MRK 876 (48795 s)	1.17	3559	585	6.08 ± 0.35	2.10	4831	806	5.99 ± 0.30

NOTE—The columns show (1) the MRC name of the SMS4 source; (2) and (6) the measured number of background counts, per pixel, where 1 pixel = $2.36''$ on a side; (3) and (7) the background-corrected number of counts C within a circle with a radius of 5 pixels; (4) and (8) the background-corrected number of counts A within an annulus with inner and outer radii of 10 and 20 pixels, respectively; (5) and (9) the extent ratio ER , with its 1σ uncertainty. Results for the point-like source MRK 876, using observations with different exposures (reported in parentheses), are shown for comparison. The significance of source extent can be evaluated by comparing the measured ER value, columns 5 and 9, to that for the model PSF that yields $ER = 5.73$ for an unresolved source.

considered energy bands and for B0103–453 by more than 30σ (in the narrow band), based in the difference between the measured and expected values of ER . Extended emission is also suggested for B0344–345, although with lower statistical significance, but higher than 3σ in both energy bands. The extent for B1953–425 is based on a very low number of counts. The remaining sources are consistent with being unresolved.

For comparison, we applied the same method to MRK 876, having a mean count rate of ~ 0.2 ct s $^{-1}$ (Moretti et al. 2005). Among the more than three hundred observations present in the *Swift* archive, we searched for a few observations with adequate exposures to obtain a net number of counts comparable with what we found for most of our sources. Furthermore, we also stacked the two observations (obsID 00050300004 and obsID 00050302001) with the longest exposures, for a total of 48795 s. As shown in Table 5, starting from the observation with the shortest exposure (obsID 00095146191, 90 s) and moving to higher exposures (obsID 00095724014, 276 s; obsID 00095724031, 1000 s), to conclude with the stack of the two longest exposures, the uncertainty range of the extent ratio gradually shrinks around the expected value $ER = 5.73$, for both the 0.5–4 keV and the 0.3–10 keV bands.

3.1.2. Radial Profile Analysis of Extended Sources

To characterize in greater detail the soft, diffuse X-ray emission, possibly extending to angular distances larger than $\approx 1'$ (see Section 3.1.1) from the X-ray centroid, we computed the X-ray radial profiles for sources with $ER < 5.73$ by more than $\simeq 3\sigma$ - B0103–453, B0344–345, B1526–423 - with sufficient S/N. For comparison, we did the same for B1017–426, one of two point-like sources in our sample, as well as for MRK 876.

To compute the X-ray radial profile, we applied XIMAGE to the stacked event file in the 0.5–4 keV band and used the PSF command, taking into account the corresponding exposure map and performing the computation up to $5'$ from the coordinates of the X-ray centroid. Before using the PSF command, we searched for spurious point-like sources within $5'$ using the DETECT command and leaving the requested S/N ratio set to the default value $S/N=2$. We removed these spurious sources using the REMOVE_SOURCES command, taking into account the exposure map and replacing for each pixel the detected number of counts with the mean background value computed over the whole detector. For the PSF command we did not correct data for background, setting its value to zero. The data were then fitted with

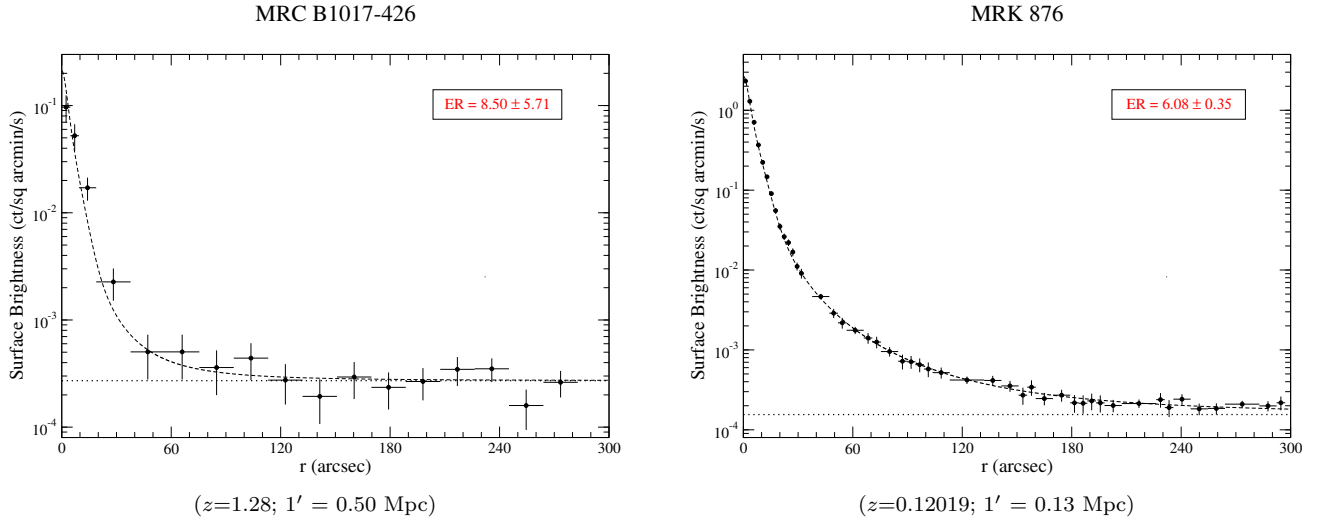


Figure 3. Radial profile in the 0.5–4 keV band of a point-like source in our sample, compared with MRK 876. For each source, the ER value is given, together with the spectroscopic redshift z and the corresponding scale factor. The dotted horizontal line represents the mean background level computed over the whole image, while the dashed line corresponds to the fit of data with the analytic model of the PSF. As discussed in the text, the radial profiles for both sources are consistent with the *Swift* PSF model.

the analytic model representing the PSF of the XRT telescope previously described, including at this step a constant value equal to the mean background computed over the whole image.

Before describing results for the extended sources, we show, in Figure 3, radial profiles for two point-like sources, B1017–426 and MRK 876, to fully validate the detailed shape of the *Swift* PSF for comparison with the extended sources in the discussion below. For MRK 876, we removed seven unrelated detections before building its radial profile with XIMAGE, while no unrelated sources were found around B1017–426. For each panel, a dotted horizontal line represents the mean background level computed over the whole image, while a dashed line corresponds to the fit of data with the analytic model of the PSF. As shown in Fig. 3, the radial profiles obtained for B1017–426 and MRK 876 agree with that expected from a point-like source ($\chi^2 = 17.0$ for $\nu = 16$ degrees of freedom for B1017–426, and $\chi^2 = 31.7$ for $\nu = 46$ degrees of freedom for MRK 876). Hence, we have validated the shape of the independently derived *Swift* PSF and can confidently compare this analytic shape to the radial profiles of the sources in our sample.

The radial profiles of the three extended sources in our sample, given in Figure 4, show both the X-ray extent and relationship to a point source. Before building these profiles, we removed three unrelated sources for B0344–345, and one unrelated source for both B1526–423 and B1953–425. The X-ray surface brightness of B0103–453 appears to be constant up to $30''$ and then decreases to the background level at $\sim 1'$. The radial profiles of B0344–345 and B1526–423 show X-ray emission extending to $\sim 2'$, but B0344–345 shows a sharp drop within $\sim 30''$ and then a steady decline, while for B1526–423, the decline is much smoother. A possible interpretation for these features is that the emission of B0344–345 might be due to the combined contribution from a brighter compact object (the core of the radio galaxy) surrounded by more tenuous emission. For B1526–423, the more uniform profile, lacking a strong central peak, suggests a relatively strong diffuse X-ray component with comparatively weak X-ray emission from any central AGN.

Of the three just described extended sources, the most interesting is B0344–345 with its large X-ray extent; the second large extended X-ray source B1526–423 is difficult to study, since it lies close to the Galactic plane. The *Swift*, WISE, GMRT, and NVSS images of B0344–345 are shown in Fig. 5. The *Swift* image shows emission extending more than $2'$ (about 120 kpc) around the central peaked X-ray emission (see also Fig. 4 for the radial profile; the mass of the associated SMBH is estimated to be $M_{BH} \approx 2.3 \times 10^8 M_{\odot}$ by [Bettoni et al. 2003](#)). As Fig. 5 shows, the radio emission is primarily extended E-W with two hot spots as well as a bright knot on the eastern side. The optical image (Fig. 5b) shows the locations of three galaxies with measured redshifts (indicated in the figure) with a full range of less than 250 km s^{-1} .

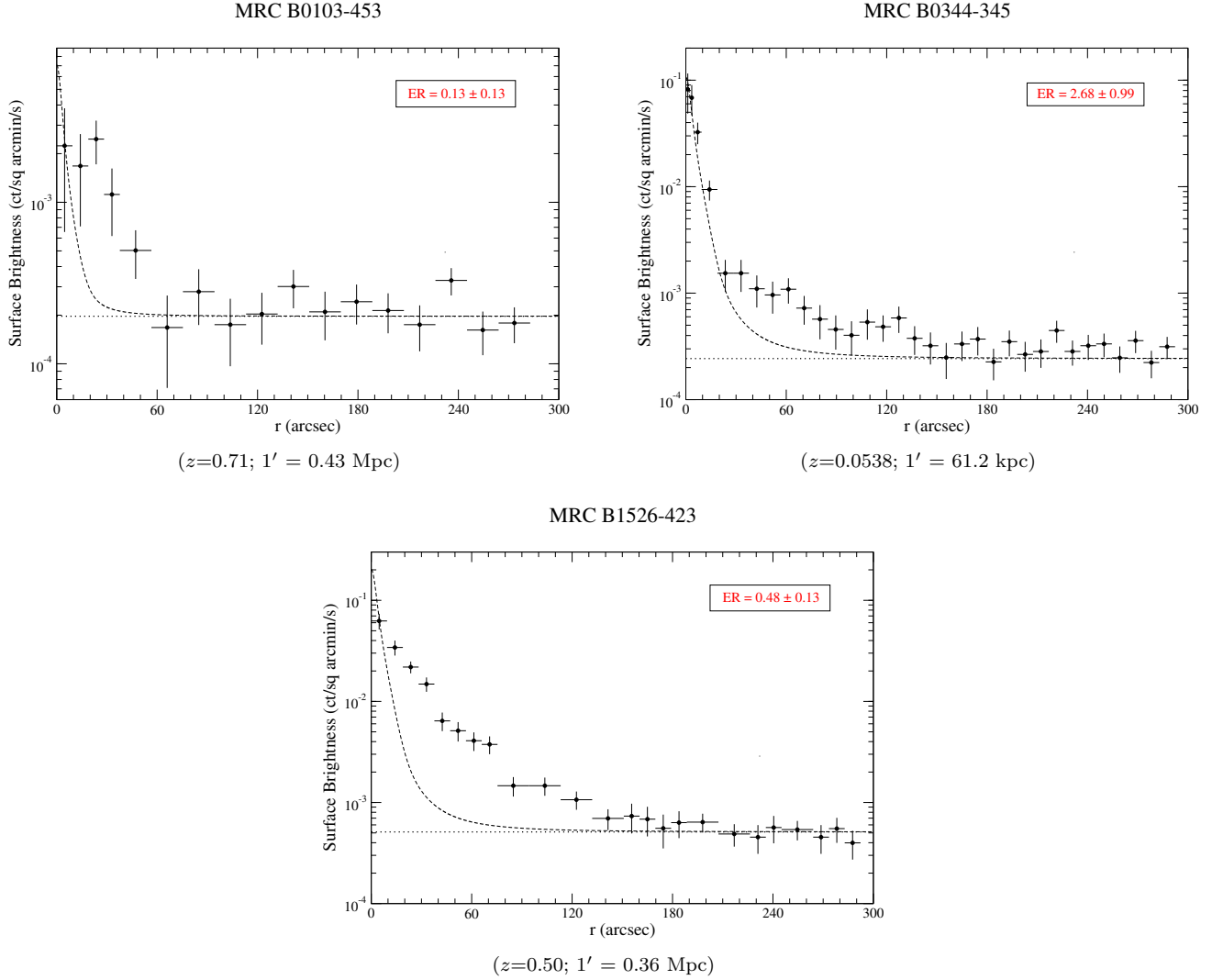


Figure 4. Radial profiles in the 0.5–4 keV band of extended SMS4 sources in our sample. For each source, the ER value is given. For all sources, the redshift z is given with the corresponding scale factor. The redshift is spectroscopic for B0344–345, and is photometric for the other two sources. The dotted horizontal line represents the mean background level computed over the whole image, while the dashed line corresponds to the fit of data with the analytic model of the PSF. As is apparent, the radial profiles confirm the extents for these three sources.

According to the results reported in Table 4, for B0344–345, the total X-ray luminosity (the central peak and the extended emission) is about 2×10^{42} ergs s^{-1} , typical of a galaxy group. Using the correlation of X-ray luminosity with temperature for thermal gas in dark matter potentials, from groups to clusters (e.g., see Zou et al. 2016 and Lovisari et al. 2020), for a luminosity of 2×10^{42} ergs s^{-1} , we would expect a cool temperature, ~ 1 keV (as noted above, there were too few source counts to fit a detailed spectrum). For such low temperature systems, poor groups or individual galaxies, with shallow potentials, compared to rich clusters, the effects of “radio mode” feedback could be significant (for discussion of radio mode feedback, in simulations as well as from galaxies to clusters, see, e.g., Croton et al. 2006; Werner et al. 2019; Nulsen et al. 2009; Hlavacek-Larrondo et al. 2022; Churazov et al. 2002).

Two graphic examples of the influence of radio mode feedback are M 87 (e.g., Forman et al. 2007) and Fornax A, aka NGC 1316 (see Kim & Fabbiano 2003; in the outskirts of the Fornax cluster) whose thermal gas atmospheres range from 2 keV (for M 87) to 0.5 keV (for Fornax A). Fornax A, with its X-ray bright central AGN and thermal extended emission (Lanz et al. 2010) is an apt comparison to B0344–345. The AGN in Fornax A has undergone a $\sim 5 \times 10^{58}$ erg outburst (Lanz et al. 2010; see also Maccagni et al. 2021 who detected outflowing gas at velocities of 2000 km s^{-1})

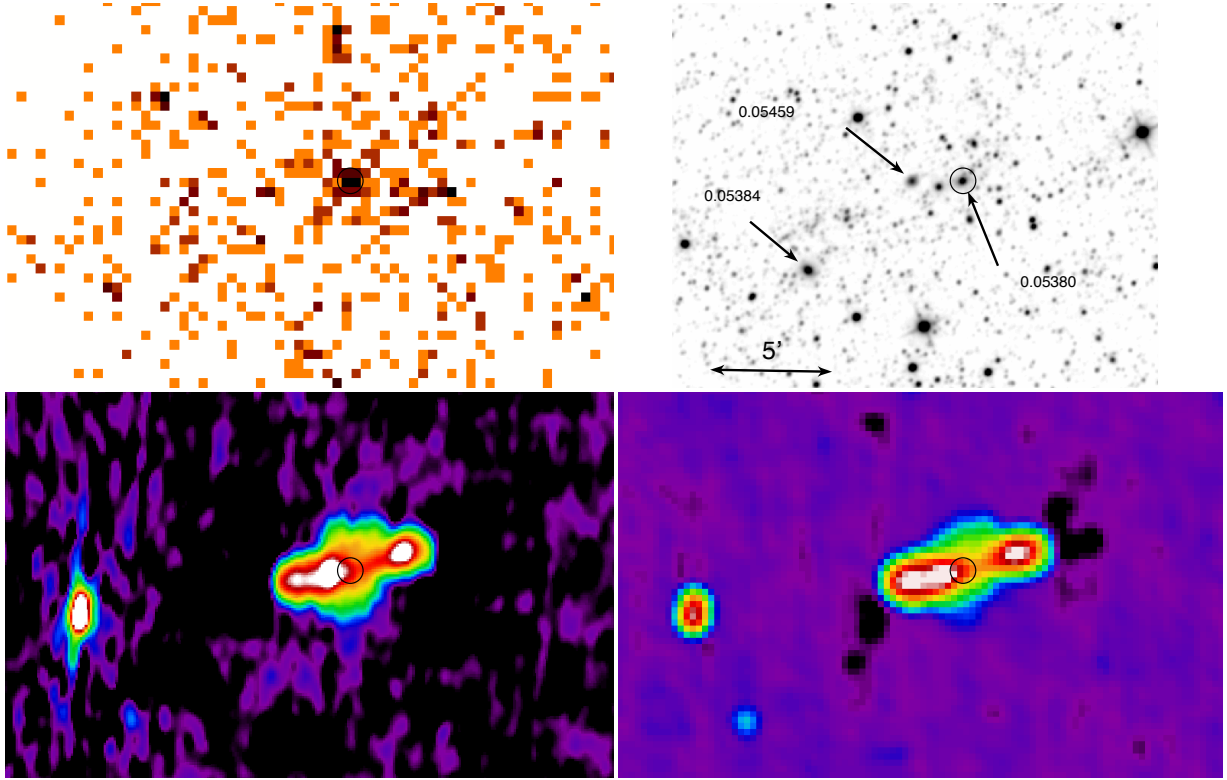


Figure 5. Images of B0344–345 (matched in scale; N is up and E to the left), (a: top left) the 11 ks *Swift* image (1-4 keV); (b: top right) WISE 3.4 μm image; (c: bottom left) GMRT survey field (153 MHz) observation; (d: bottom right) NVSS (1.4 GHz) image. The *Swift* data show emission from a compact source, presumably an AGN, as well as diffuse emission, extending about 2'. In the IR image, the three galaxies with measured redshifts (and their redshift values) are indicated. The X-ray source ID is indicated with a black circle and is included in all four images.

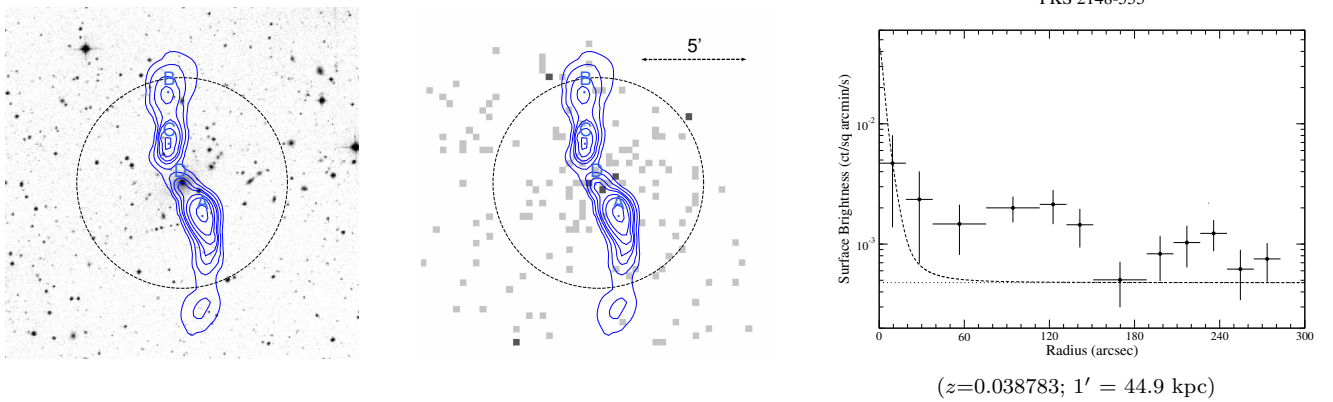


Figure 6. The extended X-ray source PKS 2148–555 (first presented in Paper I). Optical map from DSS2 (left), 0.5–4 keV X-ray map, binned by 8x8 pixels, from *Swift*-XRT (center), and the corresponding 0.5–4 keV radial profile (right). In both the optical and the X-ray maps, N is up and E is to the left. The radial profile is computed up to 5' from the X-ray centroid, corresponding to the dashed circles (note 1' = 44.9 kpc). The dotted horizontal line represents the mean background level computed over the whole image, while the dashed line corresponds to the fit of data with the analytic model of the PSF.

Table 6. Hardness ratio of the X-ray detections.

SMS4 Name	S (ct)	H (ct)	HR
(1)	(2)	(3)	(4)
B0103–453	8	14	0.27 ± 0.36
B0202–765	216	29	-0.68 ± 0.04
B0242–514	18	10	-0.29 ± 0.21
B0344–345	59	23	-0.44 ± 0.10
B0427–366	27	7	-0.59 ± 0.13
B1017–426	50	7	-0.75 ± 0.07
B1526–423	91	22	-0.61 ± 0.07
B1817–640	64	45	-0.17 ± 0.12
B1953–425	5	3	-0.25 ± 0.41
B2140–434	34	24	-0.17 ± 0.16
B2140–817	11	6	-0.29 ± 0.27

NOTE—The columns show (1) the MRC name of the SMS4 source; (2) the measured number of counts S in the soft (0.3–3 keV) band within a circle of 10 pixels ($23''.6$) centered at the coordinates of the X-ray centroid, reported in Table 2; (3) the measured number of counts H in the hard (3–10 keV) band within the same circle; (4) the hardness ratio HR , with its 1σ uncertainty.

that has strongly perturbed its hot, X-ray emitting atmosphere. Hence, deep X-ray observations of the extended, low luminosity emission around B0344–345 could provide interesting constraints on the SMBH activity and the impact of any outbursts on the surrounding thermal gas.

In Paper I, where we had not presented X-ray radial profiles, one of the most interesting extended sources was PKS 2148–555 (see Figure 6), and we expand its analysis here. In Fig. 6, we provide the source X-ray radial profile that shows emission extending to at least $\sim 3'$ (~ 100 kpc; and possibly farther). PKS 2148–555 is the BCG of the galaxy cluster A3816 (Brown & Burns 1991 and Lloyd & Jones 2002) which is itself a member of a supercluster of Abell clusters, along with A3862 and A3869 (Einasto et al. 2001). PKS 2148–555 is an FR I, as one might expect for a system in a rich environment (Wing & Blanton 2011; see also Malavasi et al. 2015; Magliocchetti et al. 2018; Kolokythas et al. 2019). The PKS 2148–555 jets exhibit numerous knots and gradual curvature as the jet traverses the ICM (see Figs. 5, 6, 9 in Lloyd & Jones 2002). As the cluster BCG and the extent of the radio jets, one should expect interesting interactions of the jet with the ambient X-ray emitting ICM in deeper X-ray images.

3.2. Hardness Ratio and Spectral Analysis

We used the COUNTS command within XIMAGE to extract the counts within circles with a radius of 10 pixels ($23''.6$), centered at the position of our X-ray detections. As adopted in Paper I, we used the two contiguous 0.3–3 keV and 3–10 keV energy bands to distinguish soft (S) and hard (H) X-ray photons. Then, we computed the hardness ratio as $HR = (H - S)/(H + S)$. As shown in Table 6, the only source that shows some evidence of hard emission, despite a considerable uncertainty, is B0103–453. For most of the remaining sources, excluding B1817–640 and B2140–434, $HR \lesssim -0.25$.

For three sources (B0202–765, B1526–423, B1817–640) we had sufficient counts to perform a full spectral analysis with XSPEC. We note that efforts to separate a compact source from surrounding thermal emission cannot be fully successful, due to scattered flux by the *Swift*-XRT optics. Hence, caution is required in evaluating the spectral fits. For B0344–345, we searched within a circle of 10 pixels ($23''.6$), that covers $\sim 80\%$ of the XRT PSF, to focus on the core of the radio galaxy and avoid contributions from the diffuse emission shown in Figure 4: despite considerable *Swift* exposure on this source, the modest count rate led to obtain only 81 counts, a value that is too low to expect precise constraints.

- **B0202–765** For this point-like source, we used the XRTPRODUCTS task to extract source events from a circle with a radius of 20 pixels ($\sim 47''$), thus covering $\sim 90\%$ of the XRT PSF, centered at the X-ray source coordinates, and background events from a circle with a radius of 50 pixels ($\sim 2'$), to avoid spurious sources. The number of events in the spectrum files corrected for the background contribution is 264, and we grouped the spectral file requiring at least 20 events per bin.

We fitted the spectrum with an absorbed power law, taking into account the spectroscopic redshift and fixing the hydrogen column density to the corresponding Galactic value (HI4PI Collaboration et al. 2016). We obtained

$\Gamma = 1.96 \pm 0.11$ and $S_{0.3-10,unabs} = 2.95_{-0.20}^{+0.29} \times 10^{-12}$ erg cm $^{-2}$ s $^{-1}$, with $\chi^2 = 12.05$ (11 d.o.f.). Uncertainties on both Γ and $S_{0.3-10,unabs}$ are given at a 1σ confidence level. Leaving the n_H parameter free to vary, we found no evidence of intrinsic absorption.

- **B1817–640** Similarly to B0202–765, also for B1817–640 we used circles with radii of $\sim 47''$ and $\sim 2'$ to extract events for the source and the background, respectively. We grouped the spectral file, with 141 events corrected for the background contribution, requiring at least 20 events per bin.

Fitting the spectrum with an absorbed power law, taking into account the spectroscopic redshift and fixing the Hydrogen column density to the corresponding Galactic value, we obtained a very poor fit ($\chi^2 = 21.5$, with 5 d.o.f.). However, leaving the n_H parameter free, we obtained a significant improvement in the χ^2 value ($\chi^2 = 7.19$, with 4 d.o.f.) with an increase in the Hydrogen column density value $n_H = 5.33_{-2.00}^{+2.56} \times 10^{22}$ cm $^{-2}$, in excess of the Galactic absorption $n_{H,Gal} = 6.79 \times 10^{20}$ cm $^{-2}$. Moreover, we were able to find $\Gamma = 1.67_{-0.50}^{+0.57}$ and $S_{0.3-10,unabs} = 1.56_{-0.54}^{+0.03} \times 10^{-12}$ erg cm $^{-2}$ s $^{-1}$. All the uncertainties are given at a 1σ confidence level.

- **B1526–423** For this extended source (see Fig. 4), we used for the source extraction region a circle with a radius of $2'$, and another circle with a radius of $3.1'$ for the background. Also in this case, we used the XRTPRODUCTS task to extract the products for the spectral analysis, this time specifying the *extended=yes* option in the task. The number of the spectral counts obtained was 371, and we grouped the data requiring at least 30 events per bin.

We fitted the spectrum with an absorbed APEC model (Smith et al. 2001), fixing the hydrogen column density to the Galactic value, the metal abundance at 0.4 Solar, and using the photometric redshift $z=0.50$. We obtained a plasma temperature $kT = 10.7_{-2.8}^{+5.6}$ keV and an unabsorbed flux $S_{0.3-10,unabs} = 2.99_{-0.27}^{+0.16} \times 10^{-12}$ erg cm $^{-2}$ s $^{-1}$, implying a luminosity $L_{0.3-10} = 2.62_{-0.20}^{+0.15} \times 10^{45}$ erg s $^{-1}$, with $\chi^2 = 11.02$ (10 d.o.f.). The uncertainties on kT , flux, and luminosity are given at a 1σ confidence level. The larger region used for the spectral analysis of B1526–423 yielded a flux more than three times larger than the value reported in Table 4, derived for a point-like source using WebPIMMS.

3.3. Comparison with other X-ray Catalogs

The Living *Swift*-XRT Point Source catalog (LSXPS, Evans et al. 2023) is a dynamic catalog that is updated almost in real time as soon as new *Swift* observations are archived. In addition to the whole catalog, two subsets (*clean* and *ultra-clean*) are found in the LSXPS. In January 2024, data from the first eROSITA All-Sky Survey (eRASS1) were released (Merloni et al. 2024). Three catalogs (*Main*, *Hard*, and *Supplementary*) are found in the First Data Release (DR1). Here we compare the results of our *Swift* campaign with the LSXPS and the eROSITA DR1 catalogs.

We searched for matching X-ray sources in the LSXPS (<https://www.swift.ac.uk/LSXPS/>) within $3'$ from the coordinates of our X-ray detections: we found at least one LSXPS source for all our detections, excluding B1953–425. As expected, we did not find any LSXPS source for all the undetected SMS4 sources listed in Table 3.

For eight of ten sources, the primary LSXPS source belongs to the *ultra-clean* sample, and is typically within $\sim 3''.5$ from the coordinates of our detections, that is comparable with the smaller positional uncertainty of our detections (see Table 2). Of the remaining two sources, 1) the extended emission of B1526–423, is incorrectly reported as four LSXPS sources within $80''$ and 2) for B2140–817, the LSXPS position is found at $8''.8$ from our position and likely incorrect in LSXPS.

For all our detected sources, we computed the angular separations d_{cl} between our detections and the LSXPS sources, as well as the matching radius $r_{cl} = (r_c^2 + r_l^2)^{1/2}$, where r_c and r_l are the positional uncertainties of corresponding sources, respectively. As shown in Table 7, we found that $d_{cl} < r_{cl}$ in all cases, excluding the noted above B2140–817. For the extended source B1526–423, we include in Table 7 only one of the two sources from the *ultra-clean* sample.

We searched in the eROSITA data archive (eRODat, <https://erosita.mpe.mpg.de/dr1/erodat/>) for 1eRASS sources matching 17 of the 18 sources in our original proposal (one of the sources, B2032–350, is not covered in the footprint of the released data). These 17 sources include B1827–360, that as of May 2024 had not been observed by *Swift*. We used the coordinates reported in Table 2 for our eleven X-ray detections and those in Table 1, corresponding to the G4Jy radio centroids, for the remaining sources.

As a result, we found a source in the *Main* (0.2–2.3 keV) catalog for nine of the eleven *Swift* detections. For the two sources (B0202–765 and B1526–423) with the highest rates detected from both *Swift* and eROSITA, a source

Table 7. Positional match with other X-ray catalogs.

SMS4 Source	LSXPS				DR1		
	r_c (arcsec)	r_l (arcsec)	r_e (arcsec)	d_{cl} (arcsec)	r_{cl} (arcsec)	d_{ce} (arcsec)	r_{ce} (arcsec)
(1)	(2)	(3)	(4)	(5)	(6)	(7)	(8)
B0103–453	4.7	5.5	...	2.2	7.2
B0202–765	3.8	3.7	1.5	0.8	5.3	1.3	4.1
B0242–514	4.8	6.6	8.5	3.3	8.2	5.0	9.9
B0344–345	4.0	2.6	5.2	1.2	4.8	2.4	6.6
B0427–366	4.8	4.7	5.6	2.4	6.7	5.4	7.4
B1017–426	4.5	4.4	4.0	0.5	6.3	2.9	6.0
B1526–423	3.8	5.4	6.2	3.1	6.6	6.1	7.3
B1754–597	8.9
B1817–640	4.0	4.5	7.4	0.7	6.0	2.6	8.4
B1953–425	5.8
B2140–434	4.3	4.4	6.8	1.8	6.2	9.1	8.0
B2140–817	5.2	6.6	10.8	8.8	8.4	3.7	12.0

NOTE—The columns show (1) the MRC name of the SMS4 source; (2) the positional uncertainty (90% c.l.) of the *Swift* detection from our campaign r_c ; (3) the positional uncertainty (90% c.l.) of the LSXPS source r_l ; (4) the positional uncertainty (90% c.l.) of the eROSITA-DE DR1 source r_e ; (5) the angular separation d_{cl} between our detection and the LSXPS source; (6) the matching radius r_{cl} between our detection and the LSXPS source; (7) the angular separation d_{ce} between our detection and the eROSITA-DE DR1 source; (8) the matching radius r_{ce} between our detection and the eROSITA-DE DR1 source.

Table 8. eROSITA-DE DR1 counterparts to SMS4 sources in our sample.

SMS4 Source	1eRASS Name	r_e	Exposure	Detection likelihood	Count Rate	0.2–2.3 keV Flux
		(arcsec)	(s)	(5)	(ct s ⁻¹)	(10 ⁻¹² erg cm ⁻² s ⁻¹)
(1)	(2)	(3)	(4)	(5)	(6)	(7)
B0202–765	J020213.5–762001	1.5	198	1549.95	1.84	1.72
B0242–514	J024344.1–511235	8.5	206	8.63	0.04	0.03
B0344–345	J034630.4–342245	5.2	257	62.45	0.11	0.10
B0427–366	J042939.9–363053	5.6	193	86.36	0.18	0.17
B1017–426	J102003.9–425130	4.0	125	86.07	0.24	0.22
B1526–423	J153014.1–423147	6.2	113	242.77	1.39	1.29
B1754–597*	J175906.4–594643	8.9	129	9.94	0.07	0.07
B1817–640	J182216.4–635917	7.4	106	11.25	0.07	0.06
B2140–434	J214334.2–431244	6.8	94	23.63	0.13	0.12
B2140–817	J214724.3–813212	10.8	159	8.81	0.03	0.03
						2.3–5.0 keV Flux
						(10 ⁻¹² erg cm ⁻² s ⁻¹)
B0202–765	J020213.5–762001	1.5	203	1576.47	1.89	2.27
B1526–423	J153014.1–423147	6.0	114	289.37	1.53	2.56

NOTE—The columns show (1) the MRC name of the SMS4 source; (2) the IAU name of the eROSITA-DE DR1 source, with (3) the positional uncertainty (90% c.l.) r_e ; (4) the exposure at the position of the source (APE_EXP_1 parameter in the DR1 catalog); (5) the detection likelihood; (6) the count rate and (7) the flux of the 1eRASS source, in the specified bands. Top: values derived from the *Main* catalog in the 0.2–2.3 keV band. Bottom: values derived from the *Hard* catalog in the 2.3–5.0 keV band.

*: This source was not detected in our campaign, due to a very short exposure.

was found also in the *Hard* (2.3–5.0 keV) catalog. The two missing sources are those for which we detected the lowest rate values, equal to (B0103–453) or lower (B1953–425) than 2×10^{-3} ct s⁻¹. The latter source is the same that was missing in the LSXPS itself, but that we were able to detect with our forced photometry. For these two sources, nothing relevant was found in the *Supplementary* catalog, with lower confidence detections.

For the six remaining sources, a detection in the *Main* Catalog was found only for B1754–597, the only source in Table 3 for which the lack of an X-ray detection in the available *Swift* data was most probably due just to the short

X-ray exposure. For the remaining five, including B1827–360, nothing relevant was found even in the *Supplementary* catalog.

Some details for the eROSITA sources, taken from the eRODat web site, are reported in Table 8. Among others, a significant parameter provided in the DR1 catalogs is the extent likelihood and the extent in arcseconds, but we did not report them in Table 8 since they were found to be 0 for all sources, excluding B1526–423.

Similarly to our analysis for the LSXPS catalog, we computed d_{ce} between our detections and corresponding eROSITA sources, as well as the matching radius $r_{ce} = (r_c^2 + r_e^2)^{1/2}$, where r_e is the positional uncertainty (90% c.l.) of eROSITA-DE DR1 sources. These values, given in Table 7, show that, overall, the consistency is excellent; only for B1240-434 is $d_{ce} > r_{ce}$, by a very small amount.

4. MULTI-FREQUENCY ANALYSIS

In this Section, we first discuss the matching of the SMS4 radio sources with the detected X-ray sources, and establish the radio/X-ray association when the radio and the X-ray positional uncertainties overlap. Using comparable values for the positional uncertainties of both radio and X-ray sources, we showed in Paper I that the probability of chance coincidence between an X-ray detection and an SMS4 source is negligible. We then discuss the WISE and optical identifications, mainly utilizing the X-ray position. The association with infrared or optical sources is allowed only if their coordinates lie within the corresponding X-ray positional uncertainty.

As also reported in Paper I, all 12 sources in our sample, detected in the X-rays, were classified by BH06 as radio galaxies (eight objects), quasars (three objects) and a quasar candidate (B0427–366). In the optical band, emission from the AGN itself, but likely also from the host galaxy, can be detected. In type II AGNs, the nuclear optical emission might be absorbed and obscured, but the infrared is more likely to reach the observer. In our efforts to localize the core of the AGN, following the same criterion already used in Paper I, with our multifrequency analysis we require a detection in both the infrared and optical bands.

As a preliminary step to match our X-ray detections with infrared and optical counterparts, we used the SkyView Virtual Observatory to retrieve infrared maps in the *W1* filter ($3.4 \mu\text{m}$) from the AllWISE Data Release (Cutri et al. 2014) Images Atlas, and optical maps in the *r* filter ($0.62 \mu\text{m}$) from the Space Telescope Science Institute (STScI) 2nd Digitized Sky Survey (DSS2). These maps are shown in Fig. 7. We used TOPCAT to cross-match our list of X-ray detections with sources from selected radio, infrared, and optical catalogs.

4.1. Associating X-ray Sources with Radio Sources

To reliably associate our 12 X-ray detected sources, listed in Table 2, with corresponding radio sources, we matched the source positions at these two energy ranges. We used G4Jy (W20) as the main matching radio catalog for the sources, that were all surveyed by GLEAM. Following W20, the typical rms positional uncertainties for G4Jy sources are $\sigma_{\alpha,S} \approx 1''.5$, $\sigma_{\delta,S} \approx 1''.7$, when their brightness-weighted centroids were computed after a cross-correlation with SUMSS data, while they are $\sigma_{\alpha,N} \approx 0''.5$, $\sigma_{\delta,N} \approx 0''.6$, when the same operation was based on NVSS data.

To match the radio and X-ray positions, we conservatively used a circular confidence region sufficiently large to ensure, with high probability, that the radio source lies within the X-ray positional uncertainty region. For this circular region, we used a radius r_X corresponding to the error radius, at 90% confidence level, for sources at the X-ray limit of sensitivity, to which we added the largest uncertainty r_r for the radio position, at the same confidence level as for the X-rays. For the X-ray band, we find $r_X = 5''.8$ from Table 2, that is the positional uncertainty of B1953–425. For the radio band, we take the larger of $\sigma_{\alpha,S}$ and $\sigma_{\delta,S}$, and multiply it by a factor of 1.645, derived from the Normal distribution, obtaining $r_r = 2''.8$.

Using a circle with $R_{90} = r_r + r_X = 8''.6$, we verified that the combined 90% confidence positional uncertainty widely overlaps - and in most cases totally includes - the corresponding G4Jy positional uncertainty for all *Swift*-XRT detections, with the exception of B0103–453 and B0344–345. As reported in Table 1, these two FR II radio galaxies are the two sources in our sample with the largest angular sizes, exceeding $2'$ (B0103–453) and even $4'$ (B0344–345); their complex radio structure is also shown in Figure 1. For both radio sources, we also noticed a mismatch between the G4Jy centroid and the coordinates of the SUMSS component that is closer to the core of the radio galaxy: as shown in Figure 7, for both SMS4 sources our *Swift* X-ray detection, and the corresponding infrared/optical counterpart that we found, lies in between the G4Jy and the SUMSS source positions. We conclude that the *Swift* X-ray observations are able to accurately determine the position of the AGN, for both B0103–453 and B0344–345, and overcome any uncertainties arising from the extended nature of the radio emission which can be significantly affected by jets, knots, and lobes, especially at lower frequencies where the radio angular resolution is sometimes limited.

Table 9. Our candidate counterparts for X-ray detected SMS4 sources.

MRC Name	Infrared Source	$W1$ (mag)	$W1 - W2$ (mag)	Optical Source	Δ (arcsec)
(1)	(2)	(3)	(4)	(5)	(6)
B0103–453	J010522.21–450517.2	14.71	1.30	S2S4040102	0.17
B0202–765	J020213.68–762003.1*	12.45	1.16	S0X7028858	0.05
B0242–514	J024344.45–511238.6*	15.04	0.37	S2TQ011216	0.77
B0344–345	J034630.57–342246.2*	12.31	0.21	S33I021144	0.01
B0427–366	J042940.12–363053.6*	14.58	1.07	S2GB002483	0.49
B1017–426	J102003.93–425130.0	14.00	1.37	S5Q2037849	0.15
B1526–423	J153014.29–423151.7	13.95	0.18	S9CT375122	0.48
B1817–640	J182216.18–635918.4*	14.90	0.79	SAQ2103623	0.21
B1953–425	J195715.25–422219.8*	15.36	1.68	SCEL082842	0.10
B2140–434	J214333.40–431253.0*	12.48	1.17	SBZ5022318	0.06
B2140–817	J214724.62–813213.0*	14.48	0.91	SAGB001072	0.75
B1754–597 [†]	J175907.08–594649.7	14.49	1.44	S7FD049277	0.35

NOTE—The columns show (1) the MRC name of the SMS4 source; (2) the AllWISE (Cutri et al. 2014) infrared source identification; (3) the AllWISE magnitude in the $W1$ filter; (4) the AllWISE $W1 - W2$ infrared color; (5) the GSC 2.4.2 (Lasker et al. 2021) optical source identification; (6) the angular separation Δ between the given infrared and optical sources.

*: this infrared source was previously associated by $W20$.

†: as discussed in the text, there are two viable counterparts for this source, detected by eROSITA. The given source IDs, lying within the X-ray positional uncertainty (see Fig. 7h) are those which include, as optical counterpart, the one consistent with BH06.

We repeated an analogous computation for B1754–597, detected only by eROSITA. Unlike the *Swift* X-ray positions, the eROSITA position with its uncertainty of $8''.9$ does not match the radio position. Using $R_{95} = 13''.9$, the combined 95% confidence positional uncertainty, does overlap the radio positional uncertainty.

4.2. Cross Matches with Infrared and Optical Catalogs

In the infrared band, the main catalog that we adopted in our cross match with the X-ray detected sources is AllWISE, and the typical positional uncertainties for our sources are in the range of 0.03–0.09 arcseconds. As in our previous paper, we took into account the infrared color of our WISE candidates, comparing $W1 - W2$ with the threshold ($W1 - W2 \geq 0.8$ mag) established by Stern et al. (2012) in their simple criterion for selecting AGNs. In the optical band, the main catalog that we used for source identification is the 2nd Generation Guide Star Catalog (GSC 2.4.2) by Lasker et al. (2021), which has a typical positional uncertainty in the 0.1–0.3 arcseconds range for our sources.

For all the 11 SMS4 sources detected by *Swift*, we find one candidate counterpart, detected in both the infrared and the optical bands. These candidates are unique, and lie within the boundaries of the X-ray positional uncertainty. While we are confident in the identification of the counterparts, not all have IR AGN colors. B0242–514, B0344–345, and B1526–423 do not lie within the AGN color range defined above; this is anomalous particularly for B0344–345 ($W1 - W2 = 0.21$ mag), since its AGN nature is quite evident from its FR II radio structure (see Fig. 1). Hence, following the same classification scheme adopted in Paper I, we define all these SMS4 sources, with unique IDs, as class A but now distinguish the three SMS4 sources (B0242–514, B0344–345, and B1526–423) lacking AGN colors as class A2, with the remaining sources as class A1.

A different situation is found for the eROSITA detected source B1754–597, for which we found two candidates: one within the X-ray uncertainty region, with AGN infrared colors, and another one outside, but close to its boundaries (see Figure 7), whose infrared counterpart is AllWISE J175905.73–594636.5, with $W1 - W2 = 0.20$ mag. This occurrence defines B1754–597 as a class B source.

All our candidate counterparts are listed in Table 9; for B1754–597, only the candidate within the uncertainty region and with AGN infrared colors is reported. As shown in column (6), the angular distance between the infrared and the optical sources is always less than $0''.8$, and only in five cases higher than $0''.25$, attesting to the fact that they can be both attributed to the same astrophysical source.

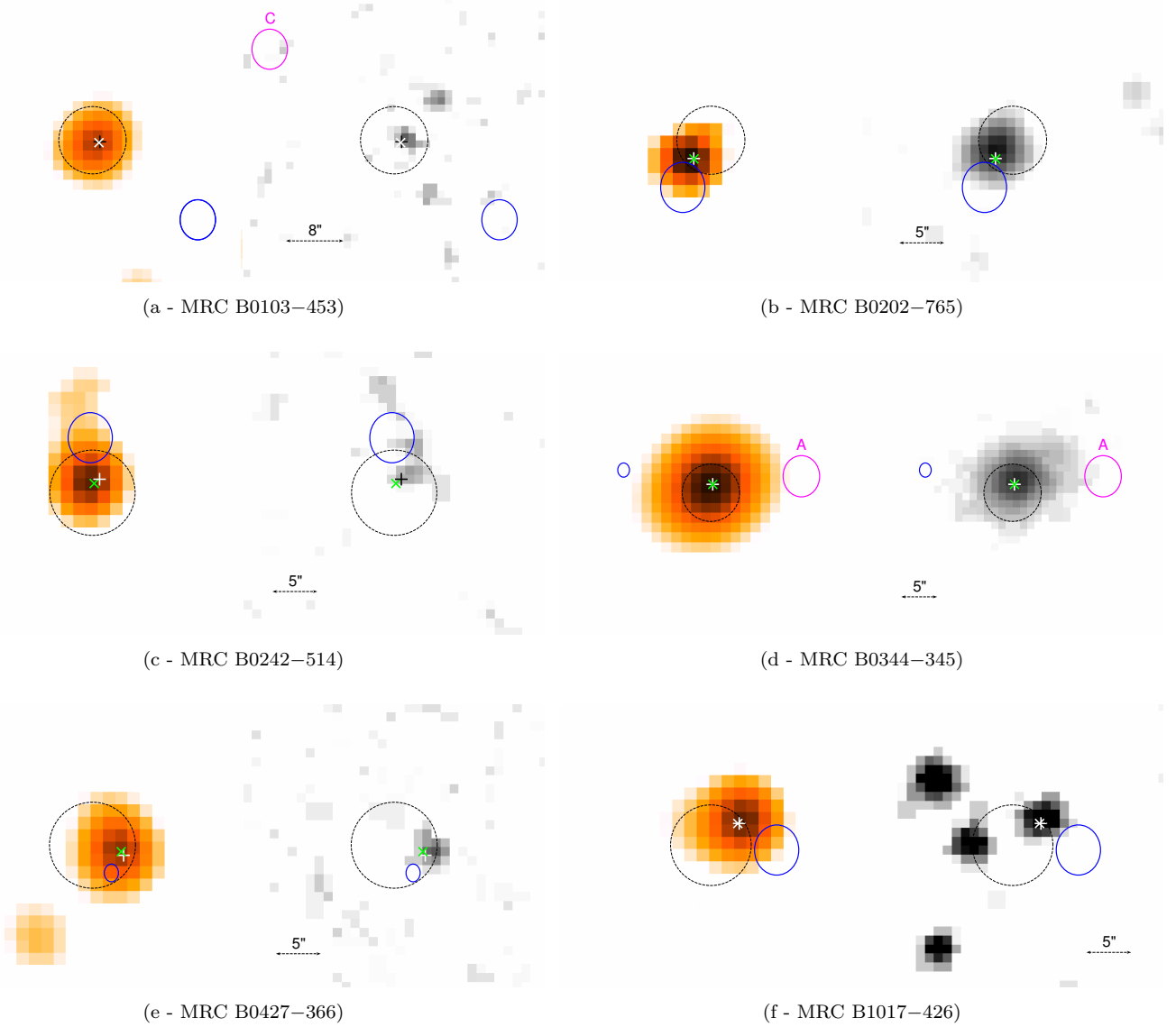


Figure 7. Infrared and optical maps, (matched in scale for each source; N is up and E is to the left), of the eleven SMS4 sources detected by *Swift*-XRT in our sample and also of B1754–597, detected by eROSITA. Infrared maps (left side of each panel) in the *W1* filter ($3.4 \mu\text{m}$) are from AllWISE, while optical maps (right side; 1 pixel= $1''$) in the *r* filter are from DSS2. Blue ellipses mark the positional uncertainty of G4Jy sources; ellipses are magenta for SUMSS components, also shown for the FR II radio galaxies B0103–453 and B0344–345, with letters corresponding to those assigned in Figure 1. Dashed circles mark the positional uncertainty of the X-ray sources; the circle is black for our *Swift*-XRT sources, and red for the 1eRASS source corresponding to B1754–597. Positional uncertainties are given at 90% confidence level for both the radio and the X-ray sources. Crosses (x) and plus signs (+) mark infrared sources from AllWISE and optical sources from GSC 2.4.2. Black or white are equally used for AllWISE and GSC 2.4.2 sources to improve the visibility with respect to the map in the background. Green is used for AllWISE counterparts also associated by W20, and for the optical counterpart of B1754–597 suggested by BH06.

4.3. Comparison with Earlier Studies

W20 associated an infrared counterpart from AllWISE to eight of the twelve SMS4 sources - including B1754–597 - for which X-ray emission was detected. More recently, AllWISE infrared counterparts for B1017–426 and B1526–423 were reported by [Massaro et al. \(2023a\)](#). As a result, with our approach, we confirm all the infrared counterparts previously addressed in the literature, and we provide for the first time AllWISE counterparts for B0103–453 and B1754–597.

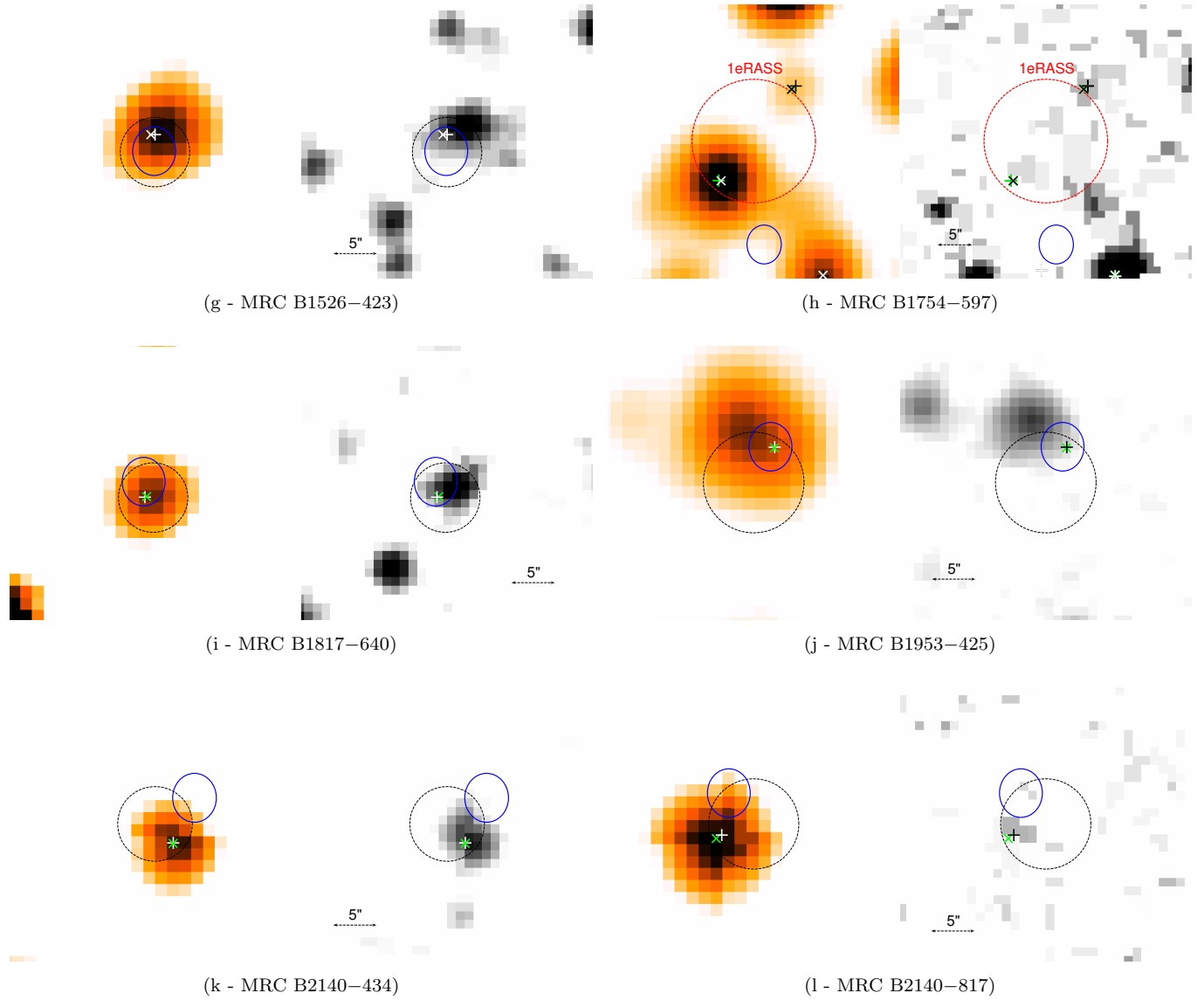


Figure 7. (*continued*)

Optical counterparts were associated by BH06 to each of the twelve X-ray detected sources, using either the plates from the UK Schmidt Southern Sky Survey or R-band CCD images from a dedicated campaign at the AAT. As shown in Table 10, we find excellent agreement between the coordinates reported in the GSC 2.4.2 catalog and those reported by BH06, with angular distances in most cases less than $1''$ (only B0202–765 and B1754–597 exceed $1''$, but are $< 2''$) leading us to conclude that both optical sources refer to the same astrophysical objects. Thus, we independently confirm all BH06 counterparts, and we list the GSC 2.4.2 sources in Table 9 for the sake of simplicity.

Comparing our optical candidates with those given more recently in Massaro et al. (2023a) (see their Table 3) and García-Pérez et al. (2024) (see their Table 1), we provide additional candidates for B0103–453 and B1754–597, the same sources mentioned earlier for the infrared band. In particular, we verified that the counterpart provided by García-Pérez et al. (2024) for B0242–514 matches the counterpart that we give in Table 9, with an angular separation of $1''.3$. We also note that, for B1953–425, the angular separation between our optical counterpart and that given by Massaro et al. (2023a) exceeds $5''.5$, and therefore might refer to a different source.

Table 10. Comparison between optical counterparts.

MRC Name	GSC 2.4.2 Source		Burgess & Hunstead (2006b)		
	R.A. (J2000) (^h ^m ^s)	Decl. (J2000) (^o ' ^{''})	R.A. (J2000) (^h ^m ^s)	Decl. (J2000) (^o ' ^{''})	Δ (arcsec)
(1)	(2)	(3)	(4)	(5)	(6)
B0103–453	01 05 22.20	–45 05 17.1	01 05 22.12	–45 05 17.1	0.88
B0202–765	02 02 13.69	–76 20 03.1	02 02 13.41	–76 20 04.7	1.92
B0242–514	02 43 44.39	–51 12 38.2	02 43 44.40	–51 12 37.9	0.31
B0344–345	03 46 30.58	–34 22 46.2	03 46 30.52	–34 22 45.8	0.85
B0427–366	04 29 40.11	–36 30 54.1	04 29 40.05	–36 30 54.3	0.72
B1017–426	10 20 03.92	–42 51 30.0	10 20 03.85	–42 51 30.2	0.79
B1526–423	15 30 14.25	–42 31 51.7	15 30 14.25	–42 31 51.5	0.21
B1817–640	18 22 16.21	–63 59 18.5	18 22 16.21	–63 59 18.7	0.16
B1953–425	19 57 15.26	–42 22 19.8	19 57 15.31	–42 22 19.1	0.92
B2140–434	21 43 33.41	–43 12 53.0	21 43 33.36	–43 12 52.2	0.94
B2140–817	21 47 24.34	–81 32 12.6	21 47 24.52	–81 32 12.9	0.48
B1754–597*	17 59 07.13	–59 46 49.7	17 59 07.25	–59 46 48.9	1.22

NOTE—The columns show (1) the MRC name of the SMS4 source; (2) the Right Ascension (J2000) and (3) the Declination (J2000) of the GSC 2.4.2 source that we give as optical counterpart (see Table 9); (4) the Right Ascension (J2000) and (5) the Declination (J2000) of the optical counterpart given by Burgess & Hunstead (2006b) (see their Table 7); (6) the angular separation Δ with respect to the corresponding GSC 2.4.2 source.

*: this source was detected in the X-rays by eROSITA.

5. SMS4 SOURCES STILL UNOBSERVED WITH NARROW FOV INSTRUMENTS

Since 2015, we successfully proposed two observational campaigns to improve the X-ray coverage of the SMS4 sample of 137 bright radio sources using *Swift* snapshot observations. As we began our program, 57 sources had existing *Chandra*, *XMM-Newton*, or *Swift* data (seven only by *Swift*), leaving 80 sources that lacked pointed moderate/high resolution observations. In Paper I we discussed 31 sources, including seven targets previously observed by *Swift*. Thus, with 17 radio sources presented in the current paper, our *Swift* campaigns observed half (41) of the sources that were not previously observed in X-rays.

Considering that one source, B2223–528, was observed by *Chandra* in November 2022, 38 sources from the original sample still lack dedicated, pointed observations. We searched in the DR1 *Main* Catalog for these 38 SMS4 sources, using the coordinates of the corresponding G4Jy sources. We followed the same procedure described in Section 4.1 to compute the matching radius R between the radio and the X-ray sources. As R_X , we adopted the highest positional uncertainty (90% c.l.) of the 1eRASS sources with the shortest angular distance from the coordinates of each G4Jy source. Using the X-ray positional uncertainty found for B1136–320, $R_X = 12''.2$. Adopting for R_r the same value reported in Section 4.1, we obtain $R=15''$: with this value, we find 18 SMS4 sources so far detected by eROSITA. The list of these SMS4 sources, reported in Table 11, provides the corresponding 1eRASS source, that is the likely X-ray counterpart from the eROSITA DR1 Catalog.

Finally, considering 4 sources (B2049–368, B2115–305, B2226–386, and B2259–375) lying outside the eROSITA-DE footprint, 16 SMS4 sources are undetected by eROSITA in the DR1.

6. SUMMARY

In the current paper, we present a final set of 17 objects from our sample⁴ of radio sources, selected in Paper I as having high flux density at 181 MHz, and observed since May 2022 as part of a second *Swift* observational campaign (PI Maselli). As a whole, considering both *Swift* campaigns, the number of SMS4 sources in the *Swift* archive increased by 41 sources (30% of the SMS4 sample).

Following Paper I, for each source we carried out a local source detection to derive source intensity and significance (see Section 3). We detected 11 sources (see Table 2), four of which were also detected by Massaro et al. (2023b). For all the *Swift* detected sources we derived their X-ray properties, including extent and hardness ratio.

⁴ One of the 17 was not detected by *Swift*, but is found in the eROSITA survey. One additional source from our *Swift* proposal, B1827–360, remains unobserved.

Table 11. eROSITA-DE DR1 likely counterparts to SMS4 Sources Unobserved by Narrow FOV Instruments.

SMS4 Source	G4Jy ID	1eRASS Name	r_e (arcsec)	Exposure (s)	Detection likelihood	Count Rate (ct s ⁻¹)	0.2–2.3 keV Flux (10 ⁻¹² erg cm ⁻² s ⁻¹)
(1)	(2)	(3)	(4)	(5)	(6)	(7)	(8)
B0003–833	12	J000617.3–830608	8.1	184	12.76	0.04	0.04
B0036–392	70	J003826.5–385946	3.8	100	83.15	0.28	0.26
B0119–634	145	J012140.3–630900	1.6	182	584.87	0.87	0.81
B0251–675	301	J025155.6–671759	1.6	278	803.04	0.80	0.75
B0646–398	629	J064811.1–395711	5.8	180	39.81	0.10	0.09
B0658–656	636	J065813.1–654453	2.3	866	281.35	0.13	0.12
B0719–553	653	J072015.4–552521	4.6	301	104.90	0.17	0.16
B1123–351	917	J112552.6–352341	7.1	145	23.00	0.11	0.10
B1136–320	934	J113916.8–322229	12.2	138	10.00	0.05	0.05
B1215–457	986	J121806.2–460028	2.3	183	354.33	0.57	0.53
B1421–382	1157	J142416.4–382648	0.8	173	2564.57	3.51	3.26
B1756–663	1455	J180118.1–662305	8.2	148	7.15	0.05	0.05
B1840–404	1505	J184428.8–402159	7.7	78	41.14	0.27	0.25
B2150–520	1740	J215408.3–515013	8.1	91	7.44	0.06	0.06
B2201–555	1756	J220504.8–551732	6.3	100	16.90	0.09	0.08
B2226–411	1781	J222918.6–405125	6.3	93	40.04	0.19	0.18
B2252–530	1797	J225548.9–524547	10.7	99	6.38	0.04	0.04
B2332–668	1843	J233510.7–663658	2.5	151	307.68	0.61	0.57

NOTE—The columns show (1) the MRC name of the SMS4 source; (2) the corresponding G4Jy ID; (3) the IAU name of the eROSITA-DE DR1 source, with (4) the positional uncertainty (90% c.l.) r_e ; (5) the exposure at the position of the source (APE_EXP_1 parameter in the DR1 catalog); (6) the detection likelihood; (7) the count rate and (8) the flux of the 1eRASS source, in the specified band.

To investigate source extent, we carried out a simple ratio test (see Section 3.1.1 and Table 5 for details), that uses the ratio of source counts in a circle with radius $\sim 12''$ divided by the source counts in the annulus $\sim 24\text{--}48''$. This ratio was then compared to that expected for an unresolved source, derived from the *Swift* PSF. We found two sources, B0103–453 and B1526–423, to be clearly extended and, at lower significance, B0344–345 to be likely extended. The remaining sources are consistent with point-like emission.

In addition to the analysis performed in Paper I, for the three sources mentioned above, we generated their radial profiles (see Section 3.1.2, and Fig. 4) to characterize their extent up to $5'$ from the X-ray centroid. The X-ray emission for B0344–345 and B1526–423 extends to at least $2'$ (see Fig. 4). For B0103–453, despite lower S/N compared to the two sources above, X-ray emission extends to at least $1'$ (see Fig. 4).

Since we did not characterize source extent in Paper I, we present in Fig. 6 the radial profile of the very extended emission for PKS 2148–555, along with a radio map superposed on the DSS2 image. As a result, in both our *Swift* campaigns, described in Paper I and in the current paper, we were able to characterize the extended nature of six sources. For comparison, from eROSITA DR1, only B1526–423 and PKS 2148–555 are given as extended in the DR1 catalogs, and with a much smaller extent than found in our analysis.

Hardness ratio analysis (see Section 3.2) reveals that the two point-like sources, B0202–765 and B1017–426, as well as a few other sources with robust statistics such as B0427–366 and B1526–423, are characterized by soft X-ray emission. The HR value of one source, B0103–453, an extended source, instead suggests hard emission, but a higher S/N would be needed to strengthen conclusions for this source, as well as for the remaining sources. Despite a count rate exceeding 10^{-2} ct s⁻¹ for five of our X-ray detections (B0202–765, B1017–426, B1526–423, B1817–640, and B2140–434), none of them is found in any catalog of hard X-ray sources.

We performed a spectral analysis (see Section 3.2 for details) for three sources with adequate S/N, adopting a power law model for B0202–765 and B1817-640, and a thermal plasma emission model for the extended source B1526–423. For B0202–765, we obtained a photon index $\Gamma = 1.96^{+0.19}_{-0.19}$ and an unabsorbed flux $S_{0.3-10,unabs} = 2.95^{+0.39}_{-0.36} \times 10^{-12}$ erg cm⁻² s⁻¹, with no evidence of intrinsic absorption. A column density in excess to the Galactic value was instead found for B1817–640, with $n_H = 5.33^{+2.56}_{-2.00} \times 10^{22}$ cm⁻². For B1526–423, we found a plasma temperature $kT = 10.7^{+5.6}_{-2.8}$ keV but, as we noted earlier (see Section 3.2), there may be some contamination from scattered photons from a central AGN. The luminosity that we found for this source is $L_{0.3-10} = 2.62^{+0.15}_{-0.20} \times 10^{45}$ erg s⁻¹.

In late January 2024, data products from 1eRASS were published (Merloni et al. 2024), enabling a first comparison of our *Swift* snapshots with results obtained by eROSITA. The eROSITA DR1 catalogs listed 10 of the 17 SMS4 sources of our sample, with nine from the *Swift* detected sources and one (B1754–597) not detected by *Swift*. Also, the one source in our sample that was not observed with *Swift*, B1827–360, was not detected by eROSITA.

In Section 4, we matched the twelve X-ray detections (eleven from *Swift* and one from DR1) with the AllWISE and the GSC 2.4.2 catalogs to search for infrared and optical counterparts. As in Paper I, we required a detection in both the infrared and the optical bands to establish a counterpart at lower frequencies for our X-ray detections. As a result, we were able to establish a single candidate counterpart for eleven of the twelve X-ray detections. Only for the source detected by eROSITA did we find a second, possible (but less likely) candidate. Comparing our results with the counterparts previously proposed by W20 and BH06, our analysis, relying on X-ray source positions, independently confirms the eight infrared counterparts provided by W20 and all twelve optical counterparts provided by BH06.

For all four sources for which W20 did not provide an infrared counterpart in their G4Jy sample, we identify an AllWISE source; the same infrared source was given by Massaro et al. (2023a) for B1017–426 and B1526–423, and in addition we provide infrared counterparts for B0103–453 and B1754–597. As regards the optical band, we provide a counterpart for these same two sources (B0103–453 and B1754–597) in addition to those reported by Massaro et al. (2023a) and García-Pérez et al. (2024), and also suggest a different optical counterpart for B1953–425 with respect to Massaro et al. (2023a).

As reported in Section 5, among the 38 SMS4 sources still lacking pointed X-ray observations, 18 are already detected in the eROSITA DR1 catalogs, 16 are in the DE footprint but not yet detected, and four lie outside the DE footprint.

In conclusion, this second paper completes our analysis, from our two *Swift* campaigns, of the *Swift*-XRT observations of bright radio sources in the southern hemisphere, comparable to the 3C sample in the north. As described above, these include notably interesting sources - bright across the spectrum from radio to X-ray - that remain poorly studied but have promise for detailed investigations.

The authors thank the referee for a careful reading of the paper and for very helpful comments that improved the paper. They also thank the *Swift* PI, Brad Cenko, his deputies, and the Science Operations Team for performing the requested observations. W.F., C.J., and R.K. acknowledge support from the Smithsonian Institution and the Chandra High Resolution Camera Project through NASA contract NAS8-03060. A.M. acknowledges financial support from the ASI-INAF agreement No. 2022-14-HH.0. This work has been partially supported by the ASI-INAF program I/004/11/4. This research has made use of archival data, software or online services provided by the ASI Space Science Data Center (SSDC); the High Energy Astrophysics Science Archive Research Center (HEASARC) provided by NASA’s Goddard Space Flight Center; the SIMBAD database operated at CDS, Strasbourg, France; the NASA/IPAC Extragalactic Database (NED) operated by the Jet Propulsion Laboratory, California Institute of Technology, under contract with the National Aeronautics and Space Administration; the NASA/IPAC Infrared Science Archive, which is funded by the National Aeronautics and Space Administration and operated by the California Institute of Technology.

Facilities: *Swift* (XRT), SkyView Virtual Observatory (<https://skyview.gsfc.nasa.gov/current/cgi/query.pl>), IRSA.

REFERENCES

- Baade, W., & Minkowski, R. 1954a, ApJ, 119, 206, doi: [10.1086/145812](https://doi.org/10.1086/145812)
- . 1954b, ApJ, 119, 215, doi: [10.1086/145813](https://doi.org/10.1086/145813)
- Bennett, A. S. 1962, MmRAS, 68, 163
- Bettoni, D., Falomo, R., Fasano, G., & Govoni, F. 2003, A&A, 399, 869, doi: [10.1051/0004-6361:20021869](https://doi.org/10.1051/0004-6361:20021869)
- Bottacini, E. 2022, MNRAS, 515, 3174, doi: [10.1093/mnras/stac1890](https://doi.org/10.1093/mnras/stac1890)
- Brown, D. L., & Burns, J. O. 1991, AJ, 102, 1917, doi: [10.1086/116012](https://doi.org/10.1086/116012)
- Burgess, A. M., & Hunstead, R. W. 2006a, AJ, 131, 100, doi: [10.1086/498677](https://doi.org/10.1086/498677)
- . 2006b, AJ, 131, 114, doi: [10.1086/498679](https://doi.org/10.1086/498679)
- Burrows, D. N., Hill, J. E., Nousek, J. A., et al. 2005, SSRv, 120, 165, doi: [10.1007/s11214-005-5097-2](https://doi.org/10.1007/s11214-005-5097-2)
- Chiaberge, M., Gilli, R., Lotz, J. M., & Norman, C. 2015, The Astrophysical Journal, 806, 147, doi: [10.1088/0004-637X/806/2/147](https://doi.org/10.1088/0004-637X/806/2/147)
- Churazov, E., Brüggén, M., Kaiser, C. R., Böhringer, H., & Forman, W. 2001, ApJ, 554, 261, doi: [10.1086/321357](https://doi.org/10.1086/321357)

- Churazov, E., Forman, W., Jones, C., & Böhringer, H. 2000, *A&A*, 356, 788, doi: [10.48550/arXiv.astro-ph/0002375](https://doi.org/10.48550/arXiv.astro-ph/0002375)
- Churazov, E., Sunyaev, R., Forman, W., & Böhringer, H. 2002, *MNRAS*, 332, 729, doi: [10.1046/j.1365-8711.2002.05332.x](https://doi.org/10.1046/j.1365-8711.2002.05332.x)
- Condon, J. J., Cotton, W. D., Greisen, E. W., et al. 1998, *AJ*, 115, 1693, doi: [10.1086/300337](https://doi.org/10.1086/300337)
- Croton, D. J., Springel, V., White, S. D. M., et al. 2006, *MNRAS*, 365, 11, doi: [10.1111/j.1365-2966.2005.09675.x](https://doi.org/10.1111/j.1365-2966.2005.09675.x)
- Cutri, R. M., Wright, E. L., Conrow, T., et al. 2014, *VizieR Online Data Catalog*, II/328
- Dicken, D., Tadhunter, C., Axon, D., et al. 2012, *ApJ*, 745, 172, doi: [10.1088/0004-637X/745/2/172](https://doi.org/10.1088/0004-637X/745/2/172)
- Dunkley, J., Komatsu, E., Nolta, M. R., et al. 2009, *ApJS*, 180, 306, doi: [10.1088/0067-0049/180/2/306](https://doi.org/10.1088/0067-0049/180/2/306)
- Edge, D. O., Shakeshaft, J. R., McAdam, W. B., Baldwin, J. E., & Archer, S. 1959, *MmRAS*, 68, 37
- Einasto, M., Einasto, J., Tago, E., Müller, V., & Andernach, H. 2001, *AJ*, 122, 2222, doi: [10.1086/323707](https://doi.org/10.1086/323707)
- Evans, P. A., Page, K. L., Beardmore, A. P., et al. 2023, *MNRAS*, 518, 174, doi: [10.1093/mnras/stac2937](https://doi.org/10.1093/mnras/stac2937)
- Event Horizon Telescope Collaboration, Akiyama, K., Alberdi, A., et al. 2019, *ApJL*, 875, L1, doi: [10.3847/2041-8213/ab0ec7](https://doi.org/10.3847/2041-8213/ab0ec7)
- Fabian, A. C., Sanders, J. S., Taylor, G. B., et al. 2006, *MNRAS*, 366, 417, doi: [10.1111/j.1365-2966.2005.09896.x](https://doi.org/10.1111/j.1365-2966.2005.09896.x)
- Fabian, A. C., Sanders, J. S., Ettori, S., et al. 2000, *MNRAS*, 318, L65, doi: [10.1046/j.1365-8711.2000.03904.x](https://doi.org/10.1046/j.1365-8711.2000.03904.x)
- Forman, W., Jones, C., Churazov, E., et al. 2007, *ApJ*, 665, 1057, doi: [10.1086/519480](https://doi.org/10.1086/519480)
- García-Pérez, A., Peña-Herazo, H. A., Jimenez-Gallardo, A., et al. 2024, *ApJS*, 271, 8, doi: [10.3847/1538-4365/ad159e](https://doi.org/10.3847/1538-4365/ad159e)
- Gehrels, N., Chincarini, G., Giommi, P., et al. 2004, *ApJ*, 611, 1005, doi: [10.1086/422091](https://doi.org/10.1086/422091)
- HI4PI Collaboration, Ben Bekhti, N., Flöer, L., et al. 2016, *A&A*, 594, A116, doi: [10.1051/0004-6361/201629178](https://doi.org/10.1051/0004-6361/201629178)
- Hilbert, B., Chiaberge, M., Kotyla, J. P., et al. 2016, *ApJS*, 225, 12, doi: [10.3847/0067-0049/225/1/12](https://doi.org/10.3847/0067-0049/225/1/12)
- Hlavacek-Larrondo, J., Li, Y., & Churazov, E. 2022, in *Handbook of X-ray and Gamma-ray Astrophysics* (Springer), 5
- Hurley-Walker, N., Callingham, J. R., Hancock, P. J., et al. 2017, *MNRAS*, 464, 1146, doi: [10.1093/mnras/stw2337](https://doi.org/10.1093/mnras/stw2337)
- Israel, F. P. 1998, *A&A Rv*, 8, 237, doi: [10.1007/s001590050011](https://doi.org/10.1007/s001590050011)
- Kim, D.-W., & Fabbiano, G. 2003, *ApJ*, 586, 826, doi: [10.1086/367930](https://doi.org/10.1086/367930)
- Kolokythas, K., O'Sullivan, E., Intema, H., et al. 2019, *MNRAS*, 489, 2488, doi: [10.1093/mnras/stz2082](https://doi.org/10.1093/mnras/stz2082)
- Laing, R. A., Riley, J. M., & Longair, M. S. 1983, *MNRAS*, 204, 151, doi: [10.1093/mnras/204.1.151](https://doi.org/10.1093/mnras/204.1.151)
- Lanz, L., Jones, C., Forman, W. R., et al. 2010, *ApJ*, 721, 1702, doi: [10.1088/0004-637X/721/2/1702](https://doi.org/10.1088/0004-637X/721/2/1702)
- Large, M. I., Mills, B. Y., Little, A. G., Crawford, D. F., & Sutton, J. M. 1981, *MNRAS*, 194, 693, doi: [10.1093/mnras/194.3.693](https://doi.org/10.1093/mnras/194.3.693)
- Lasker, B., Lattanzi, M. G., McLean, B. J., et al. 2021, *VizieR Online Data Catalog*, I/353
- Lilly, S. J., & Longair, M. S. 1984, *MNRAS*, 211, 833, doi: [10.1093/mnras/211.4.833](https://doi.org/10.1093/mnras/211.4.833)
- Lilly, S. J., Longair, M. S., & McLean, I. S. 1983, *Nature*, 301, 488, doi: [10.1038/301488a0](https://doi.org/10.1038/301488a0)
- Lloyd, B. D., & Jones, P. A. 2002, *MNRAS*, 331, 717, doi: [10.1046/j.1365-8711.2002.05239.x](https://doi.org/10.1046/j.1365-8711.2002.05239.x)
- Longair, M. S., & MacDonald, G. H. 1969, *MNRAS*, 145, 309, doi: [10.1093/mnras/145.3.309](https://doi.org/10.1093/mnras/145.3.309)
- Longair, M. S., & Pooley, G. G. 1969, *MNRAS*, 145, 121, doi: [10.1093/mnras/145.2.121](https://doi.org/10.1093/mnras/145.2.121)
- Lovisari, L., Schellenberger, G., Sereno, M., et al. 2020, *ApJ*, 892, 102, doi: [10.3847/1538-4357/ab7997](https://doi.org/10.3847/1538-4357/ab7997)
- Lynds, R. 1970, *ApJL*, 159, L151, doi: [10.1086/180500](https://doi.org/10.1086/180500)
- Maccagni, F. M., Serra, P., Gaspari, M., et al. 2021, *A&A*, 656, A45, doi: [10.1051/0004-6361/202141143](https://doi.org/10.1051/0004-6361/202141143)
- Magliocchetti, M., Popesso, P., Brusa, M., & Salvato, M. 2018, *MNRAS*, 478, 3848, doi: [10.1093/mnras/sty1309](https://doi.org/10.1093/mnras/sty1309)
- Malavasi, N., Bardelli, S., Ciliegi, P., et al. 2015, *A&A*, 576, A101, doi: [10.1051/0004-6361/201425155](https://doi.org/10.1051/0004-6361/201425155)
- Maselli, A., Forman, W. R., Jones, C., Kraft, R. P., & Perri, M. 2022, *ApJS*, 262, 51, doi: [10.3847/1538-4365/ac87a5](https://doi.org/10.3847/1538-4365/ac87a5)
- Massaro, F., White, S. V., García-Pérez, A., et al. 2023a, *ApJS*, 265, 32, doi: [10.3847/1538-4365/acaf05](https://doi.org/10.3847/1538-4365/acaf05)
- Massaro, F., White, S. V., Paggi, A., et al. 2023b, *ApJS*, 268, 32, doi: [10.3847/1538-4365/ace1f5](https://doi.org/10.3847/1538-4365/ace1f5)
- Mauch, T., Murphy, T., Buttery, H. J., et al. 2003, *MNRAS*, 342, 1117, doi: [10.1046/j.1365-8711.2003.06605.x](https://doi.org/10.1046/j.1365-8711.2003.06605.x)
- Merloni, A., Lamer, G., Liu, T., et al. 2024, *arXiv e-prints*, arXiv:2401.17274, doi: [10.48550/arXiv.2401.17274](https://doi.org/10.48550/arXiv.2401.17274)
- Moretti, A., Campana, S., Mineo, T., et al. 2005, in *Society of Photo-Optical Instrumentation Engineers (SPIE) Conference Series*, Vol. 5898, UV, X-Ray, and Gamma-Ray Space Instrumentation for Astronomy XIV, ed. O. H. W. Siegmund, 360–368
- Nulsen, P., Jones, C., Forman, W., et al. 2009, in *American Institute of Physics Conference Series*, Vol. 1201, *The Monster's Fiery Breath: Feedback in Galaxies, Groups, and Clusters*, ed. S. Heinz & E. Wilcots (AIP), 198–201
- Puccetti, S., Capalbi, M., Giommi, P., et al. 2011, *A&A*, 528, A122, doi: [10.1051/0004-6361/201015560](https://doi.org/10.1051/0004-6361/201015560)

- Schmidt, M. 1963, *Nature*, 197, 1040,
doi: [10.1038/1971040a0](https://doi.org/10.1038/1971040a0)
- Schreier, E. J., Burns, J. O., & Feigelson, E. D. 1981, *ApJ*,
251, 523, doi: [10.1086/159492](https://doi.org/10.1086/159492)
- Smith, R. K., Brickhouse, N. S., Liedahl, D. A., &
Raymond, J. C. 2001, *ApJL*, 556, L91,
doi: [10.1086/322992](https://doi.org/10.1086/322992)
- Stern, D., Assef, R. J., Benford, D. J., et al. 2012, *ApJ*,
753, 30, doi: [10.1088/0004-637X/753/1/30](https://doi.org/10.1088/0004-637X/753/1/30)
- Tingay, S. J., Goeke, R., Bowman, J. D., et al. 2013,
PASA, 30, e007, doi: [10.1017/pasa.2012.007](https://doi.org/10.1017/pasa.2012.007)
- Wayth, R. B., Lenc, E., Bell, M. E., et al. 2015, *PASA*, 32,
e025, doi: [10.1017/pasa.2015.26](https://doi.org/10.1017/pasa.2015.26)
- Werner, N., McNamara, B. R., Churazov, E., &
Scannapieco, E. 2019, *SSRv*, 215, 5,
doi: [10.1007/s11214-018-0571-9](https://doi.org/10.1007/s11214-018-0571-9)
- White, S. V., Franzen, T. M. O., Riseley, C. J., et al.
2020a, *PASA*, 37, e018, doi: [10.1017/pasa.2020.9](https://doi.org/10.1017/pasa.2020.9)
—, 2020b, *PASA*, 37, e017, doi: [10.1017/pasa.2020.10](https://doi.org/10.1017/pasa.2020.10)
- Wing, J. D., & Blanton, E. L. 2011, *AJ*, 141, 88,
doi: [10.1088/0004-6256/141/3/88](https://doi.org/10.1088/0004-6256/141/3/88)
- Zou, S., Maughan, B. J., Giles, P. A., et al. 2016, *MNRAS*,
463, 820, doi: [10.1093/mnras/stw1992](https://doi.org/10.1093/mnras/stw1992)